Bulletin of Earthquake Engineering
https://doi.org/10.1007/s10518-024-01997-8

ORIGINAL ARTICLE

Mitigating inter-story drift concentration in seismic-resistant self-centering braced frames by using strong backup systems

Jiahao Huang[1] · **Songye Zhu**[1]

Received: 3 January 2024 / Accepted: 6 August 2024

Abstract
Seismic-resistant self-centering concentrically braced frames (SC-CBFs) are susceptible to the concentration of inter-story drifts during earthquakes owing to the relatively low energy dissipation ability of braces. To address this limitation, this study proposed a novel solution by designing a strong backup (SB) system to mitigate inter-story deformation concentration in "weak" stories. The proposed SB system consisting of truss members can be attached to the existing SC-CBF through pin connections, forming a system, termed strong backup SC-CBF (SC-CBF-SB), to promote a more uniform distribution of inter-story drifts along the height of the frame and mitigate the weak story behavior. A six-story chevron-braced frame is adopted to investigate the seismic performance of SC-CBF and SC-CBF-SB. Finite element models of SC-CBF and SC-CBF-SB are built. The mechanical characteristics and dynamic responses of the SC-CBF-SB are examined. To comprehensively evaluate the performance of both SC-CBF and SC-CBF-SB, static pushover analyses and nonlinear time-history analyses are conducted. Additionally, incremental dynamic analysis (IDA) is performed to evaluate the responses (particularly drift concentration) of both frame types subjected to increasing seismic intensity levels. Numerical results show that the maximum value of the drift concentration factor (DCF) is around 1.3 and 1.8 for SC-CBF-SB and SC-CBF, respectively, indicating that SC-CBF-SB can effectively mitigate inter-story drift concentration of SC-CBF. Meanwhile, the proposed SB system has a minimal negative impact on the favorable SC ability of the frame.

Keywords Self-centering braced frame · Inter-story drift · Strong backup system · Seismic performance · Drift concentration factor

1 Introduction

Although traditional concentrically braced frames (CBFs) have been employed as common lateral load-resistant systems (Tremblay et al. 2003; Uriz and Mahin 2008), they are associated with well-known limitations, such as limited system ductility and brace buckling

✉ Songye Zhu
songye.zhu@polyu.edu.hk

[1] Department of Civil and Environmental Engineering, The Hong Kong Polytechnic University, Hung Hom, Kowloon, Hong Kong, China

under compression. To overcome the brace buckling issue in traditional CBFs, buckling-restrained braced frames (BRBFs), featured by the stable hysteretic response and superior energy dissipation ability of braces under tension–compression cycles, have been proposed and increasingly applied in the past decades (Watanabe et al. 1988; Aiken et al. 2002; Fahnestock et al. 2007; Di Sarno and Elnashai 2009). However, the poor performance of CBFs and BRBFs in controlling residual deformation was also observed during past earthquakes (Sabelli 2001; McCormick et al. 2007). Notably, when residual deformation exceeds 0.5%, repair costs are likely higher than that of rebuilding (McCormick et al. 2008). To minimize structural residual deformation and decrease repair costs after earthquakes, the self-centering (SC) concept has been introduced into seismic-resistant structural systems (Ricles et al. 2002; Christopoulos et al. 2008; Zhu and Zhang 2008; Qiu and Zhu 2017; Lavaei et al. 2023). Currently, the most commonly adopted SC structural elements and systems include: (1) SC dampers and braces (Dolce et al. 2005; McCormick et al. 2007; Zhu and Zhang 2008; Li et al. 2018; Qiu et al. 2022; Hu et al. 2024); (2) SC beam-column connections (Garlock et al. 2005; Wolski et al. 2009; Speicher et al. 2011; Asadolahi and Fanaie 2020); (3) SC shear walls and rocking systems (Chi and Liu 2012; Eatherton et al. 2014; Razavi and Fanaie 2023), and (4) SC isolators (Casciati et al. 2007; Dolce et al. 2007; Wang et al. 2020).

Among these SC systems, self-centering concentrically braced frames (SC-CBFs) consisting of a variety of SC braces (SCBs) have recently been proposed to minimize the residual deformation of braced frames after earthquakes (Zhu and Zhang 2007; Christopoulos et al. 2008; Miller et al. 2012; Erochko et al. 2013). The current fabrication strategy for SCBs involves utilizing either post-tensioned methods (e.g., post-tension tendons) or special alloy materials (e.g., shape memory alloys, SMAs) to produce a representative flag-shaped hysteretic behavior that realizes the SC and energy dissipation abilities simultaneously. For example, Christopoulos et al. (2008) proposed an SCB design consisting of two bracing members, pre-tensioned fiber elements, energy dissipation elements, and a series of guiding elements, wherein the elongation of the fiber elements was activated by any relative motion between the two bracing members, providing the desirable SC forces. They validated its SC behavior through full-scale axial tests, wherein a 2.17-m long SCB provided tensile and compressive forces of around 800 kN. The proposed SCB could be installed in frame structures by a means similar to conventional steel braces. They also performed dynamic loading tests of a partially braced frame. Wang et al. (2021) developed an SCB prototype consisting of a group of disc springs and an additional friction device and evaluated its effectiveness in the seismic control of frame responses through numerical analyses. The disc springs were used to provide reliable SC ability, where different stack patterns could lead to various combinations of load resistance and deformability. They validated its SC behavior through full-scale axial tests, wherein a 1.85-m long SCB provided tensile and compressive forces of about 300 kN. Zhu and Zhang (2008) and Qiu and Zhu (2017) investigated the performance of a CBF equipped with novel SMA-based SCBs. SMAs constitute a unique class of metal alloys that exhibit superelasticity, energy dissipation capabilities, and high corrosion resistance (Chen and Zhu 2024). The superelasticity enables SMAs to recover their initial shapes after removing the external load, resulting in an ideal flag-shaped hysteretic response. The SMA-based SCB consists of interior and exterior segments that slide relative to each other, and the axial loads (either tension or compression) always stretch the SMA wires in this design.

However, as frequently reported in the past literature (Qiu and Zhu 2016,; Wang et al. 2021, 2023; Lin et al. 2022; Zhang et al. 2022), SC-CBFs exhibit a pronounced concentration of inter-story drifts during earthquakes, mainly attributed to the relatively lower

energy dissipation ability and limited post-yielding stiffness of SCBs. For example, Qiu and Zhu (2016) reported that SC-CBFs exhibited less uniform distribution of inter-story drift ratios than BRBFs when designed with the same elastic properties, yield strength, and post-yield stiffness. Similarly, Wang et al. (2023) conducted nonlinear time history analyses of BRBFs and SC-CBFs and observed that the weaker energy dissipation capability of SC-CBFs leads to unexpected drift concentration. Unlike ideal conditions with a uniform distribution of inter-story drifts along the height of the frame, the inter-story drift concentration in "weak stories" may occur in practical conditions. Notably, "weak stories" hereinafter do not really mean that the stiffness and strength of some stories are under-designed. In fact, the occurrence locations of weak stories are quite random under different seismic ground motions. In these "weak stories", the deformation demands may exceed the capacities of braces designed following uniform drift distributions, whereas the inter-story drifts of other stories could be considerably smaller than those in weak stories. Such non-uniform profiles of inter-story drift may also intensify the P–Δ effect in weak stories, thereby causing greater damage and even increasing the risk of structural collapse.

Notably, the inter-story concentration is also commonly observed in CBFs and BRBFs (Sabelli et al. 2003; Uriz and Mahin 2008; Qiu and Zhu 2016). To address this issue, several solutions have been proposed by researchers, such as the implementation of an elastic truss system and a stiff rocking core. For example, Lai and Mahin (2015) proposed a strongback system, which was essentially an augmented braced bay in the original braced frame, to prevent the occurrence of weak stories in CBFs. Comparative analyses between the original and strongback frames showed that the strongback system could effectively prevent the occurrence of deformation concentration. Later on, Simpson and Mahin (2018) conducted cyclic tests and numerical analyses on a full-scale two-story BRBF retrofitted with an augmented braced bay and proved the effectiveness of the strongback system. Pollino et al. (2017) proposed to introduce a stiff rocking core into an existing CBF to redistribute lateral demands and prevent soft-story responses. Qu et al. (2014) conducted nonlinear static pushover analyses on low-rise (three-story) and medium-rise (six-story) CBFs equipped with stiff rocking cores and illustrated the efficacy of rocking cores in reducing the concentration of inter-story deformation. Moreover, Qu et al. (2015) investigated the dynamic responses of CBFs rehabilitated using rocking cores subjected to seismic ground motions. Slovenec et al. (2017) conducted a hybrid test on a 1/3-scale prototype CBF rehabilitated with a stiff rocking core. Ebrahimi Majumerd et al. (2023) developed a base-rocking dual-core braced-frame system to mitigate the concentration of inter-story deformation.

Previous upgrading approaches mainly focused on improving the seismic performance and mitigating weak stories in conventional CBFs and BRBFs. Nonetheless, there has been limited research on strategies to address the issue of weak-story behavior in SC-CBF structures. Moreover, existing upgrading approaches require either significant alterations to the internal structures of the original buildings or the construction of external rocking systems outside of the original buildings, demanding substantial labor, material, and space costs. In view of these facts, this paper proposes a novel type of strong backup (SB) truss system to overcome the weak-story behavior observed in SC-CBFs. The proposed SB system can be attached to an existing SC-CBF via pin connections to form a strong backup SC-CBF (SC-CBF-SB) system. Compared with the previous upgrading approaches, the proposed SB system does not alter the internal structures of the original buildings or require large space around the structure, which has good compatibility with existing structural systems. The quasi-static and dynamic behaviors of the SC-CBF-SB are explored in this study. To comprehensively understand the performance of SC-CBF-SB, static pushover and nonlinear dynamic analyses of SC-CBF and SC-CBF-SB are performed and compared

systematically. In particular, to evaluate the dynamic responses (including inter-story drift concentration) of both frames subjected to increasing seismic intensity levels, incremental dynamic analysis (IDA) is performed. The numerical analyses successfully demonstrate the effectiveness of the proposed SB system in mitigating weak-story behavior in SC-CBF, meanwhile having minimal negative impact on the desirable SC ability of the frame.

2 Working mechanism of SB system

As aforementioned, a variety of SCBs have been developed in the literature. These SCBs are typically characterized by a flag-shaped hysteretic loop and show similar seismic behavior. Figure 1a depicts a representative SC-CBF considered in this study, wherein SCBs may be one of any aforementioned SCB examples in Sect. 1. As shown in Fig. 1a, the typical distribution pattern of inter-story drifts of SC-CBF often exhibits concentrated deformation in one or a few stories under seismic motions (Qiu and Zhu 2016).

As shown in Fig. 1b, the proposed SB system functions as a hinged truss system, consisting of vertical, horizontal, and diagonal members. The SB system is connected to one column of the SC-CBF through pin connections at each story and pinned at its base, thereby enabling a pivotal motion of the SB system around the pinned base. In contrast to previous upgrading techniques, the proposed SB system obviates the modifications to the original interior structures and has a simpler configuration, and occupies less space needed than those of existing rocking cores. Meanwhile, the SB system is designed to maintain essentially elastic throughout the whole earthquake process, enabling the redistribution of story shear demands and promoting a uniform profile of inter-story drifts along the frame height. Unlike the distribution pattern in Fig. 1a, b demonstrates the improved distribution pattern of the inter-story drifts of SC-CBF-SB, where drifts are uniformly distributed with the incorporation of the SB system. Different from a conventional braced frame where braces are designed to dissipate energy, the SB system is intended to remain nearly elastic during seismic events. To achieve

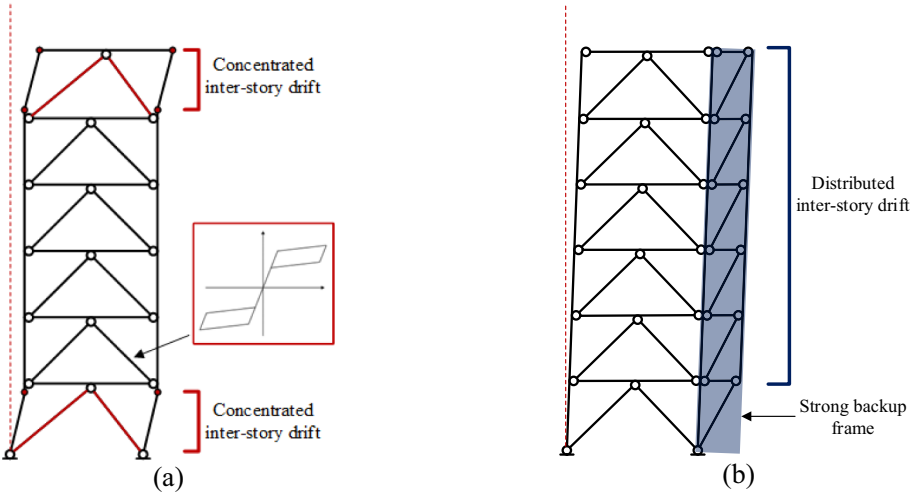

Fig. 1 Illustration of the distribution pattern of inter-story drift ratios of **a** SC-CBF and **b** SC-CBF-SB

this objective, the SB system is designed using the simplified modal pushover analysis method (Simpson and Rivera Torres 2021). This approach considers the combination of force demands from the first and higher modes and ensures the SB system remains nearly elastic under all modes of excitation.

3 Prototype frame

A six-story steel braced frame with SCBs is adopted to investigate the behavior of SC-CBF and SC-CBF-SB. The adopted six-story steel braced frame with BRBs was initially designed by Sabelli et al. (2003) and later modified to an SC-CBF by replacing BRBs with SCBs by Qiu and Zhu (2016). The SC-CBF frame incorporates a chevron-braced configuration. Notably, several SCBs (e.g., post-tension-based and SMA-based SCBs) show nearly symmetrical tension and compression behavior, minimizing unbalanced lateral force demand on the beams. Therefore, only 5% unbalanced bracing force is considered in the beam design. Story height of the first story is defined as 5.5 m and that of the other stories is 4 m. The bay width is 9 m. The tributary masses for each bay of the braced frame are 151.0 ton for the first to fifth floors and 136.5 ton for the roof. Other detailed information regarding the frame can be obtained from the reference (Sabelli et al. 2003). In the SC-CBF, all beam-column connections are designed as pin connections, and continuous columns are along the building height with pinned base connections. The same frame members as the original design by Sabelli et al. (2003) are utilized, except that BRBs are replaced by SCBs with the same values of initial stiffness and yield strength. The post-yield stiffness ratio of SCB is set as $\alpha = 0.01$, and the energy dissipation capacity is set as $\beta = 0.5$. The SC-CBF-SB consists of two parts: the main frame and the SB frame. The main frame remains identical to the SC-CBF, while the SB frame is attached to one column of the main frame via pin connections at each story and pinned at its base. The bay width of the SB system is set as 1.5 m, determined after parametric studies that are omitted herein for conciseness. In actual engineering scenarios, the width of the bay needs to be determined based on the existing structural conditions. The vertical member in the SB frame remains continuous along the height of the SB frame, whereas the horizontal and diagonal members are all pin-connected members. To facilitate construction, the vertical and horizontal members in the SB frame are designed to have the same cross-section size as the column and beam members in the main frame. Additionally, the diagonal member is selected based on the primary design goal to maintain the SB frame in an elastic state under all modes of excitation, following the simplified modal pushover analysis method proposed by Simpson and Rivera Torres (2021), which combines the responses of multiple modes obtained from the pushover analyses to estimate force demands for the designed SB frame. The flowchart of the design method is shown in Fig. 2. The method begins with an eigenvalue analysis to determine the structure's mode shapes and periods. For each significant mode, a nonlinear static pushover analysis is performed using a lateral load pattern proportional to the mode shape. The modal responses are combined using a modal combination rule to estimate the total seismic response. The following nonlinear dynamic analyses confirm that the SB frame remains elastic. Table 1 lists the major information of structural members in SC-CBF and SC-CBF-SB, including column and beam sections, initial stiffness k_i and yielding strength F_y of the braces in SC-CBF in each story, and different truss members in the SB system.

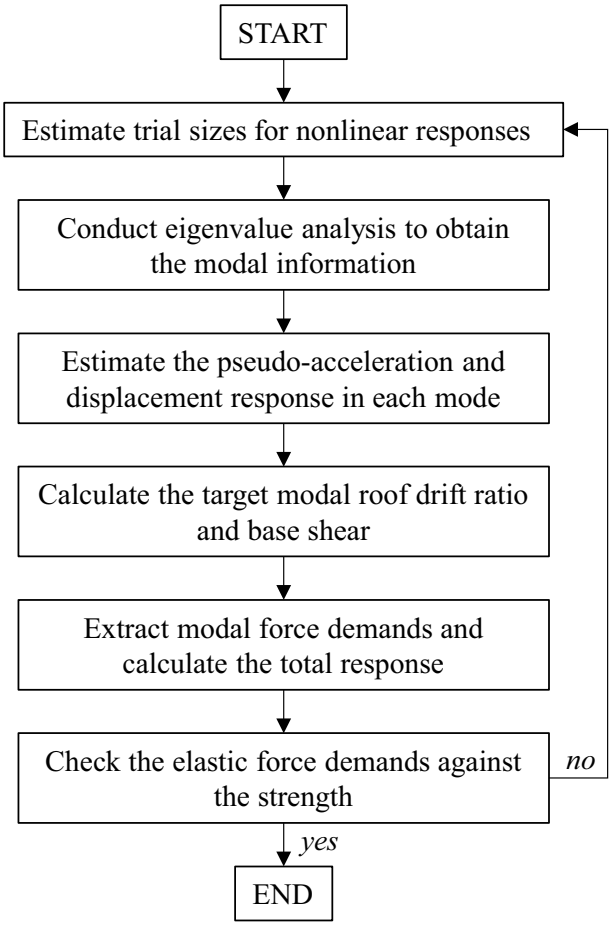

Fig. 2 Flowchart of the simplified design method based on modal pushover analysis

Table 1 Member sizes of SC-CBF and SB system

Story	SC-CBF				SB system		
	Columns	Beams	Braces		Vertical members	Horizontal members	Diagonal members
			F_y (kN)	k_i (kN /m)			
6	W14×132	W14×48	394	0.734E+05	W14×132	W14×48	W14×132
5	W14×132	W14×48	711	1.326E+05	W14×132	W14×48	W14×132
4	W14×132	W14×48	961	1.793E+05	W14×132	W14×48	W14×132
3	W14×211	W14×48	1161	2.165E+05	W14×132	W14×48	W14×132
2	W14×211	W14×48	1306	2.435E+05	W14×132	W14×48	W14×132
1	W14×211	W14×48	1704	2.878E+05	–	W14×48	W14×132

4 Numerical models

Finite element (FE) models of the two-dimensional prototype SC-CBF and SC-CBF-SB were built in OpenSees (OpenSees 2013) to investigate their seismic performance. In the SC-CBF model, the beams, columns, and braces are simulated by using the forceBeamColumn elements with fiber sections. The columns are modeled to be continuous throughout the height of the frames and have pinned connections at their bases. All beam-to-column connections are modeled as pin connections. Pin connections are also modeled at the ends of every brace. The beam and column elements are constructed from ASTM A992 steel, which has an assumed post-yield stiffness ratio of 0.003. The simulation does not take into account the degradation of steel materials resulting from local buckling as well as low-cycle fatigue. The material type of the beam and column members are defined as *Steel02*. Since the occurrence of brace buckling under compression is not permitted in this study, each brace is simulated using a single element. The cross sections of the braces are constructed by assembling uniaxial fibers. Each brace cross-section consists of a total of 16 fibers. The material type of the braces is defined as *SelfCentering* to simulate the SC behavior of SCBs, as shown in Fig. 3. The force–deformation relationship of the *SelfCentering* material is characterized by the initial stiffness k_e, yield force F_y, post-yield stiffness ratio $\alpha = 0.01$, and energy dissipation capacity $\beta = 0.5$. In SC-CBF-SB, horizontal, vertical, and diagonal members in the SB system are simulated by the forceBeamColumn elements, with their material type defined as *Steel02* as well. The vertical member is continuous along the height of the SB system, whereas the horizontal and diagonal members are modeled with hinged connections. One end of the diagonal member in the first story is pinned at the base. The Rayleigh damping of 5% is considered for the first and second modes. An idealized leaning column is modeled to carry the tributary floor mass. To avoid introducing extra lateral stiffness to the main frame, the leaning columns in each story are inter-connected through pin connections and pinned at the base. In this way, the horizontal and vertical displacements of the leaning column in each story are coupled with the corresponding story in the main frame. A large value of vertical strength and stiffness is assumed for the leaning column. Consequently, the leaning column could simulate the *P-Δ* effect but does not provide lateral stiffness to the main frame. The FE models of SC-CBF and SC-CBF-SB are shown in Fig. 4.

The multiple natural periods of the SC-CBF and SC-CBF-SB are listed in the Table 2. The first modal period of SC-CBF is approximately 0.81 s, which is quite close to the first modal period of SC-CBF-SB at approximately 0.80 s. As for the second modal period,

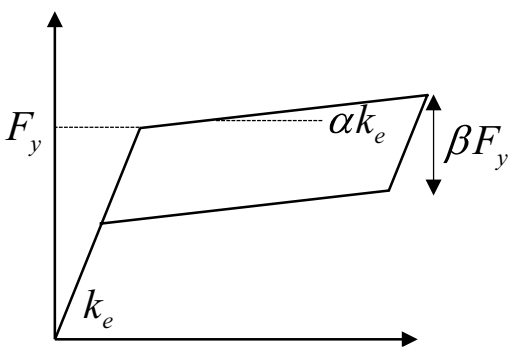

Fig. 3 Schematic of *SelfCentering* element

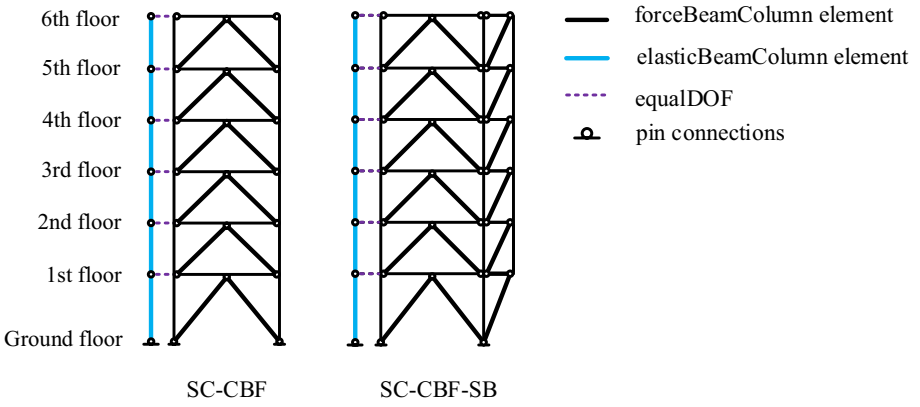

Fig. 4 FE models of SC-CBF and SC-CBF-SB in OpenSees

Table 2 Fundamental periods of SC-CBF and SC-CBF-SB

Frame type	T_1 (s)	T_2 (s)	T_3 (s)
SC-CBF	0.81	0.31	0.20
SC-CBF-SB	0.80	0.28	0.18

SC-CBF exhibits a period of approximately 0.31 s, whereas SC-CBF-SB demonstrates a shorter period of approximately 0.28 s. The SB system tends to have a rigid-body rotation around its hinge base, which approximately follows the first mode shape pattern. Therefore, the SB system does not contribute any stiffness to the first-mode motion and does not alter the first-mode period obviously. However, the second-mode and third-mode periods of SC-CBF-SB are obviously reduced by 9.6% and 10%, respectively, compared to SC-CBF, because the SB system contributes the stiffness to alter the second and third mode shapes.

5 Pushover analysis

Monotonic and cyclic pushover analyses are performed to investigate the relationships between the roof drift ratio and base shear of two frames, i.e., SC-CBF and SC-CBF-SB. The profile of the inter-story drift ratio is determined by the distribution of seismic forces along the building height (Qu et al. 2013). While the first-mode loading pattern is widely adopted in seismic design and analysis, it may not accurately represent actual seismic force distributions during severe earthquakes. Therefore, additional pushover analyses with different loading patterns are necessary to paint a more comprehensive picture of the inter-story drift distribution. Therefore, the first-mode, second-mode, and uniform loading patterns are used in the pushover analyses (Goel and Chopra 2004), where the second-mode pattern examines the high-mode effect and the uniform loading pattern is selected based on FEMA 356 (2000).

Figure 5 demonstrates the base shear versus roof drift ratio relationships of SC-CBF and SC-CBF-SB with the first-mode loading pattern. The yielding of braces among different stories during the pushover analysis is marked with red dots. Under the first-mode loading pattern, the slope of the curves of SC-CBF and SC-CBF-SB are almost the same, and the initial elastic stiffnesses of the two frames are close to each other, implying that the addition of the SB system exerts little effect on the initial elastic stiffness of the original frame. In the SC-CBF, the yielding point of the first story is far from those of upper stories: yielding of first-story braces occurs at the roof drift ratio of approximately 1.5%, whereas yielding of braces of other stories occurs when the roof drift ratio is approximately 0.3%. By contrast, in the SC-CBF-SB, the yielding points of all six stories are quite close to each other, meaning that the braces of six stories yield at almost the same moment when the roof drift ratio is about 0.3%. The deviation among the inter-story drift ratios is quite small.

Figure 6 illustrates the base shear versus roof drift ratio relationship under the second-mode loading pattern. In the SC-CBF, the sixth-story braces yield at a base shear force of about 760 kN. On the other hand, in the SC-CBF-SB, the braces in the sixth and fifth stories yield very closely at a base shear force of about 1500 kN, followed by the fourth-story braces at a base shear force of about 2200 kN.

Figure 7 presents the monotonic pushover results of SC-CBF and SC-CBF-SB under the uniform loading pattern. In the SC-CBF, the yielding points of braces in different stories exhibit significant deviations, indicating a non-uniform distribution of the inter-story drift ratio along the frame height. The first- and second-story braces yield first at the roof drift

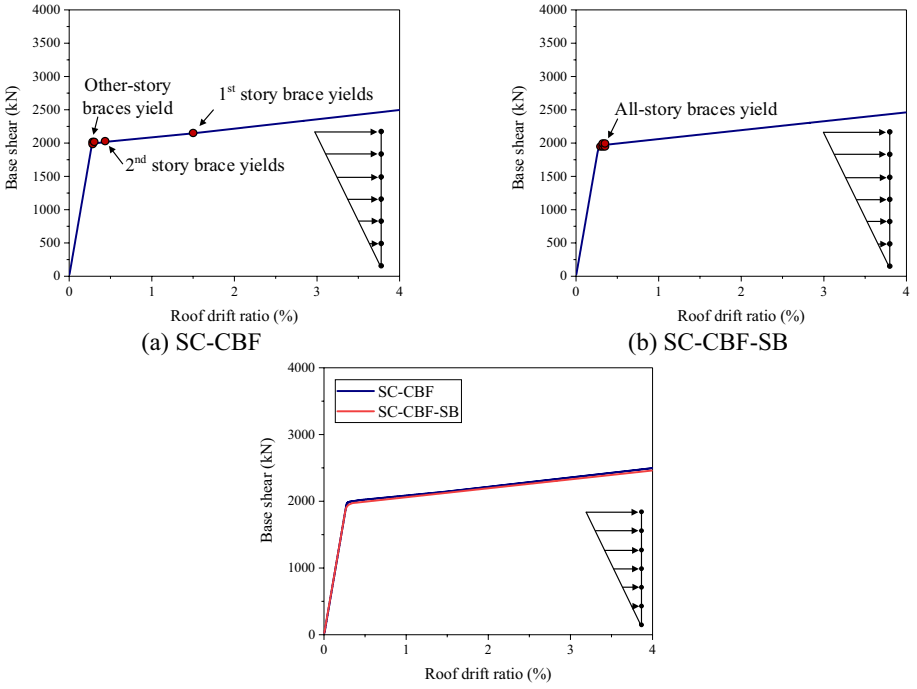

(a) SC-CBF

(b) SC-CBF-SB

(c) Comparison of SC-CBF and SC-CBF-SB

Fig. 5 Monotonic pushover analysis under lateral loads in the first-mode pattern

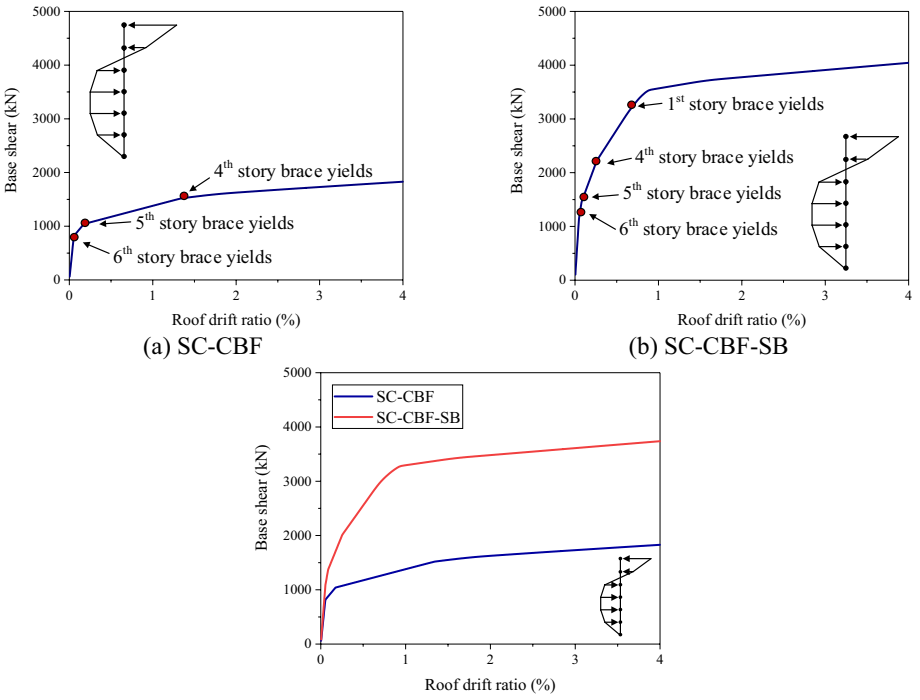

(a) SC-CBF (b) SC-CBF-SB

(c) Comparison of SC-CBF and SC-CBF-SB

Fig. 6 Monotonic pushover analysis under lateral loads in the second-mode pattern

ratio of about 0.3%, followed by braces in the third and fourth stories at 0.5% and 1%, respectively; finally, braces in the fifth and sixth stories yield at roof drift ratios of 2.25% and 3.75%, respectively. By contrast, SC-CBF-SB shows yielding points of braces within a narrow range under the uniform loading pattern, meaning that the braces in different stories yield almost at the same time.

Figure 8a shows the base shear versus roof drift ratio response subjected to cyclic pushover with the first-mode loading pattern. The elastic stiffness and post-yielding stiffness of SC-CBF-SB are almost the same as those of SC-CBF, except that the yielding base shear of SC-CBF-SB is slightly higher than that of SC-CBF, illustrating that the participation of the SB system does not affect the stiffness and energy dissipation of the original frame subjected to the first-mode loading pattern. The SB system remains elastic during the whole process.

Figure 8b exhibits the relationship between the roof drift ratios and base shear of SC-CBF and SC-CBF-SB under the second-mode loading pattern. The yielding base shear of SC-CBF-SB is considerably higher than that of SC-CBF, implying that the SB system carries a large portion of the story shear and contributes considerable story stiffness and strength under the second-mode loading pattern.

Figure 8c exhibits the relationship between the roof drift ratios and base shear of SC-CBF and SC-CBF-SB under the uniform loading pattern. The elastic stiffness of SC-CBF-SB is almost the same as that of SC-CBF. But a smaller post-yield stiffness is observed in the SC-CBF-SB.

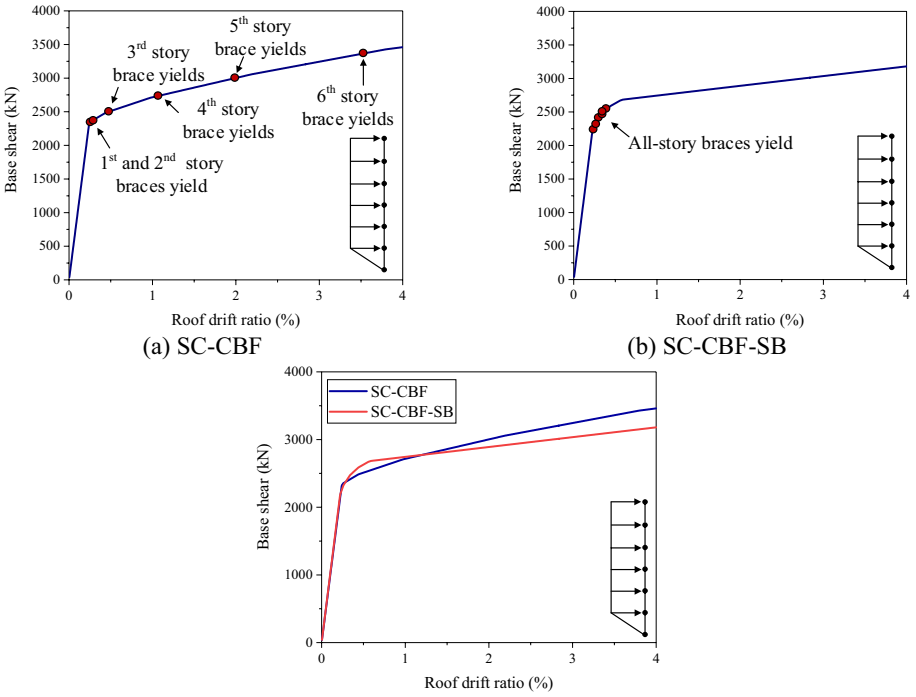

(a) SC-CBF (b) SC-CBF-SB

(c) Comparison of SC-CBF and SC-CBF-SB

Fig. 7 Monotonic pushover analysis under a uniform load pattern

Notably, the yielding forces of the braces in SC-CBF were designed according to the first-mode loading pattern, so the inter-story drift profile of SC-CBF is relatively uniform, and the yielding points of different stories are relatively close under the first-mode pattern. Consequently, the SB system mainly experiences rigid-body rotation under the first-mode loading pattern, and its contribution is insignificant. However, real seismic loads often deviate from the first-mode loading pattern or involve high-mode participation, which will lead to non-uniform inter-story drift distribution and significant inter-story drift concentration in SC-SBF, as shown in Figs. 6 and 7 under the second-mode and uniform loading patterns. In contrast, SC-SBF-SB considerably mitigates such inter-story drift concentrations, and the engagement of the SB system promotes more uniform inter-story drift profiles by re-distributing internal story shear forces along the height.

6 Ground motions

A total of 40 ground motions developed by Somerville (1997) are employed in the dynamic analyses in this paper, as shown in Table 3. These ground motions are divided into two sets, with each set containing 20 ground motions corresponding to different seismic hazard categories. The first set of ground motions, denoted by LA01-LA20, is developed for Los Angeles corresponding to exceedance probabilities of 10% in 50 years. The second set of ground motions, denoted by LA21-LA40, is developed for Los Angeles corresponding to

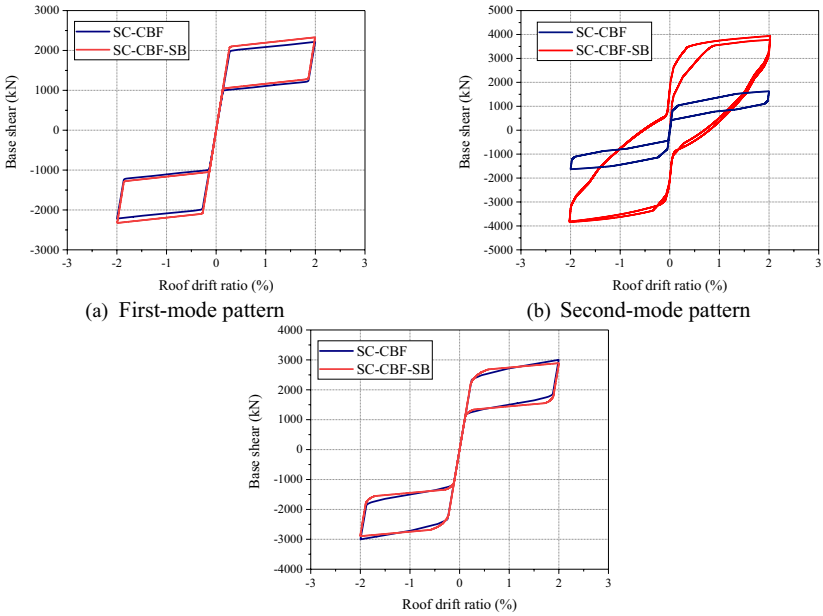

Fig. 8 Cyclic pushover analysis of the SC-CBF and SC-CBF-SB under the **a** first-mode, **b** second-mode and **c** uniform pattern

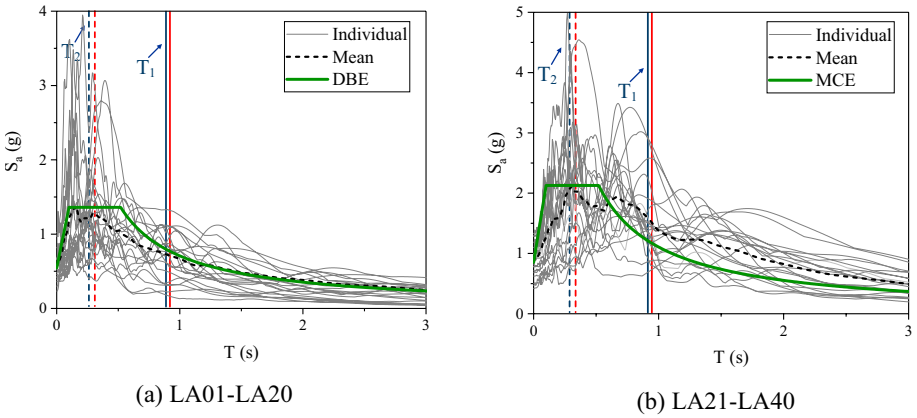

Fig. 9 Response spectrum of selected ground motions

exceedance probabilities of 2% in 50 years. Both sets of ground motions are modified from soil types S_B-S_C to soil type S_D. The geometric mean response spectrum of LA01-LA20 corresponds to the design basis earthquake (DBE), while the geometric mean response spectrum of LA21-LA40 aligns with the maximum considered earthquake (MCE). Figure 9a and b demonstrate the acceleration response spectrum together with the DBE and

Table 3 Information of the ground motions (Somerville 1997)

Name	Record	Year	Soil type	Magnitude	Mechanism	PGA (g)
LA01	Imperial Valley, El Centro	1940	Stiff	6.9	Strike slip	0.461
LA02	Imperial Valley, El Centro	1940	Stiff	6.9	Strike slip	0.676
LA03	Imperial Valley, Array #05	1979	Stiff	6.5	Strike slip	0.394
LA04	Imperial Valley, Array #05	1979	Stiff	6.5	Strike slip	0.489
LA05	Imperial Valley, Array #06	1979	Stiff	6.5	Strike slip	0.302
LA06	Imperial Valley, Array #06	1979	Stiff	6.5	Strike slip	0.235
LA07	Landers, Barstow	1992	Stiff	7.3	Strike slip	0.421
LA08	Landers, Barstow	1992	Stiff	7.3	Strike slip	0.426
LA09	Landers, Yermo	1992	Stiff	7.3	Strike slip	0.520
LA10	Landers, Yermo	1992	Stiff	7.3	Strike slip	0.360
LA11	Loma Prieta, Gilroy	1989	Stiff	7	Reverse oblique	0.665
LA12	Loma Prieta, Gilroy	1989	Stiff	7	Reverse oblique	0.970
LA13	Northridge, Newhall	1994	Stiff	6.7	Reverse	0.678
LA14	Northridge, Newhall	1994	Stiff	6.7	Reverse	0.657
LA15	Northridge, Rinaldi RS	1994	Stiff	6.7	Reverse	0.534
LA16	Northridge, Rinaldi RS	1994	Stiff	6.7	Reverse	0.580
LA17	Northridge, Sylmar	1994	Stiff	6.7	Reverse	0.570
LA18	Northridge, Sylmar	1994	Stiff	6.7	Reverse	0.817
LA19	North Palm Springs	1986	Stiff	6	Reverse	1.019
LA20	North Palm Springs	1986	Stiff	6	Reverse	0.988
LA21	Kobe	1995	Stiff	6.9	Strike slip	1.28
LA22	Kobe	1995	Stiff	6.9	Strike slip	0.92
LA23	Loma Prieta	1989	Stiff	7	Reverse oblique	0.42
LA24	Loma Prieta	1989	Stiff	7	Reverse oblique	0.47
LA25	Northridge	1994	Stiff	6.7	Reverse	0.87
LA26	Northridge	1994	Stiff	6.7	Reverse	0.94
LA27	Northridge	1994	Stiff	6.7	Reverse	0.93
LA28	Northridge	1994	Stiff	6.7	Reverse	1.33
LA29	Tabas	1974	Stiff	7.4	Reverse	0.81
LA30	Tabas	1974	Stiff	7.4	Reverse	0.99
LA31	Elysian Park (simulated)	–	Stiff	7.1	–	1.30
LA32	Elysian Park (simulated)	–	Stiff	7.1	–	1.19
LA33	Elysian Park (simulated)	–	Stiff	7.1	–	0.78
LA34	Elysian Park (simulated)	–	Stiff	7.1	–	0.68
LA35	Elysian Park (simulated)	–	Stiff	7.1	–	0.99
LA36	Elysian Park (simulated)	–	Stiff	7.1	–	1.10
LA37	Palos Verdes (simulated)	–	Stiff	7.1	–	0.71
LA38	Palos Verdes (simulated)	–	Stiff	7.1	–	0.78
LA39	Palos Verdes (simulated)	–	Stiff	7.1	–	0.50
LA40	Palos Verdes (simulated)	–	Stiff	7.1	–	0.63

MCE design spectra. The first and second periods of the SC-CBF and SC-CBF-SB are also marked in Fig. 9, in which the corresponding spectral accelerations can be extracted.

7 Nonlinear time history analyses

To comprehensively investigate the seismic performances of SC-CBF and SC-CBF-SB under seismic ground motions, nonlinear time history analyses were conducted, and the corresponding results are presented in the following two subsections. In the second part, two sets of 20 seismic motions corresponding to DBE and MCE are adopted in the dynamic analysis, which enables statistical characterization of responses under earthquakes of different intensity levels.

7.1 Performance under single ground motion

The subsection presents a case study under a selected individual ground motion LA27 (1994 Northridge, Sylmar). This case study allowed a detailed comparison between the dynamic responses of SC-CBF and SC-CBF-SB.

Figure 10 shows the time histories of inter-story drift ratios of six stories in SC-CBF and SC-CBF-SB when subjected to the ground motion LA27. Only 20-s time histories that cover the peak values of inter-story drifts are presented to have a clear view of details in the frame responses. The occurrence time of the peak inter-story drifts is marked as well. In SC-CBF, it is evident that the inter-story drifts of different stories differ considerably, and the peak inter-story drift ratios of different stories do not occur simultaneously. Specifically, the inter-story drifts of the first, second, third, and fourth stories reach their maximum values at around $t_a = 7.4$ s, while the maximum values for the fifth and sixth stories are observed at around $t_b = 9.5$ s. By contrast, in SC-CBF-SB, the inter-story drifts for all six stories are very close and reach their maximum values nearly at the same instant of $t_a = 7.4$ s.

Figure 11a and b show the distribution of the instantaneous seismic forces on SC-CBF corresponding to the two instants of 7.4 s and 9.5 s. At $t_a = 7.4$ s, the maximum inertial

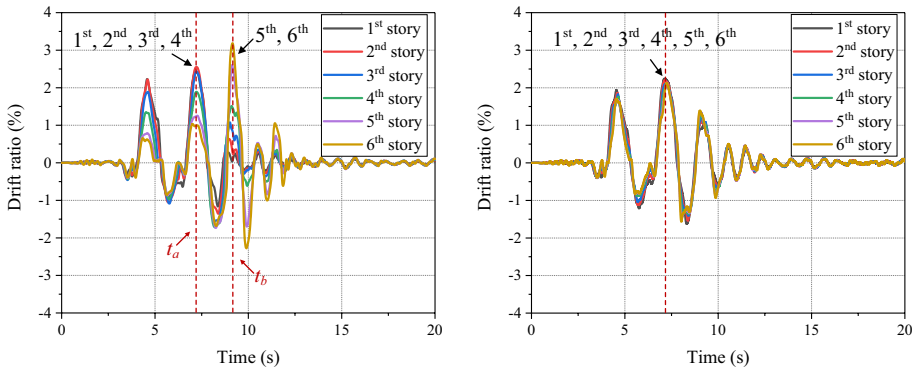

(a) SC-CBF (b) SC-CBF-SB

Fig. 10 Time history of inter-story drift ratio under the ground motion LA27

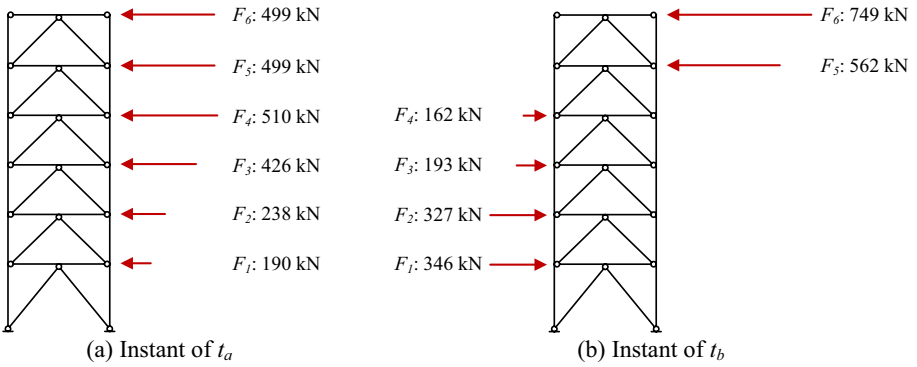

Fig. 11 Distribution of inertial forces along the SC-CBF at the two peak inter-story drift instants: **a** t_a and **b** t_b

force of 510 kN occurred at the fourth floor, leading to the occurrence of the maximum inter-story drifts in all the stories underneath; meanwhile, the inertial forces on the fifth and sixth floors are almost identical (499 kN). The lateral force distribution in Fig. 11a deviates obviously from the first-mode loading pattern assumed in the design stage. At $t_b = 9.5$ s, the directions of the inertial forces on the fifth and sixth floors are even opposite to those of the lower floors, and the maximum inertial force of 749 kN occurred on the sixth floor. The corresponding lateral force distribution shown in Fig. 11b is actually closer to the second-mode loading pattern. In comparison, Fig. 12 exhibits the distribution of the instantaneous seismic inertial forces on SC-CBF-SB at $t_a = 7.4$ s, when all the stories reach the maximum values of the inter-story drifts. The minimum inertial force of 150 kN occurred on the first floor, and the maximum inertial force of 600 kN occurred on the sixth floor of SC-CBF-SB. This observation illustrates that the SB system enforces relatively uniform profiles of lateral seismic forces and inter-story drifts within the SC-CBF-SB.

Figure 13a illustrates the distribution of the peak inter-story drifts for all six stories in both SC-CBF and SC-CBF-SB under the LA27 ground motion. In SC-CBF, the peak inter-story drifts are about 2.5% from the first to third stories; however, in the sixth story, the peak inter-story drift reached 3.2%, indicating obvious weak-story response in the upper stories of SC-CBF. By contrast, in SC-CBF-SB, the peak inter-story drifts across all six stories are close at around 2.1%, indicating that the SB system can not only effectively mitigate the weak-story behavior, but also reduce the maximum inter-story drifts among stories and minimize structural damage. Figure 13b shows the distribution of the peak absolute accelerations of SC-CBF and SC-CBF-SB. Apparently, the SC-CBF-SB frame demonstrates lower peak absolute accelerations than the SC-CBF frame, except for the sixth story where SC-CBF-SB slightly amplifies the floor acceleration. The fourth floor in the SC-CBF exhibits a peak absolute acceleration of 1.8 g, whereas it reduces to 1.2 g in the SC-CBF-SB frame. The reduced peak acceleration will lead to reduced non-structural damage in SC-CBF-SB.

Figure 14 shows the profiles of peak story shear of SC-CBF and SC-CBF-SB subjected to LA27. The story shear in SC-CBF-SB is shared by the main frame and the SB system, and both portions are illustrated in Fig. 14. Generally, the peak story shear forces in SC-CBF-SB are higher than those in SC-CBF, particularly in the first and sixth stories. For example, the peak story shear forces in the first story of SC-CBF-SB and SC-CBF are

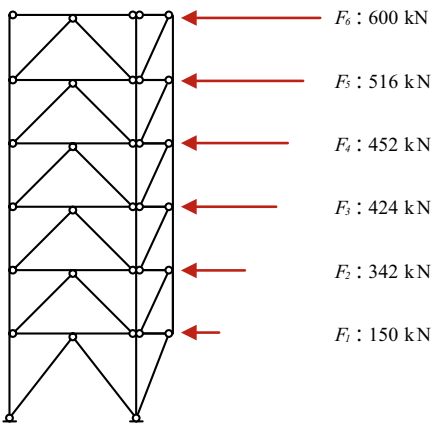

Fig. 12 Distribution of inertial forces along the SC-CBF-SB at the instant of peak inter-story drift

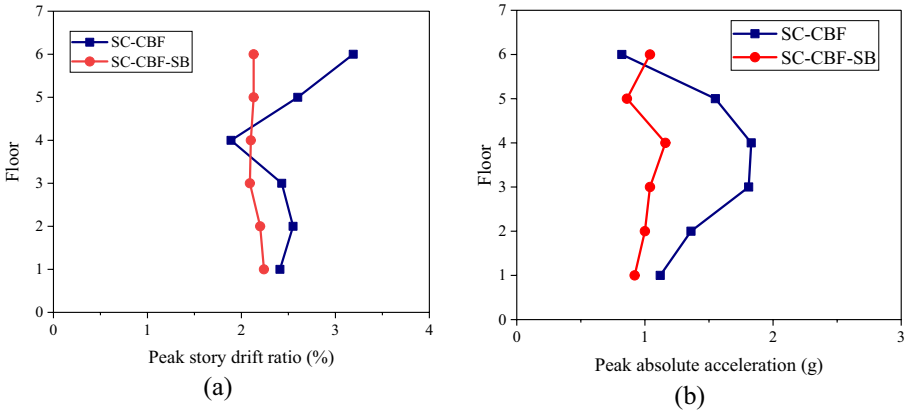

Fig. 13 Distributions of **a** peak inter-story drift ratio and **b** peak absolute acceleration when subjected to LA27

recorded as 3031 kN and 2680 kN, respectively; similarly, the peak story shear forces in the sixth story of SC-CBF-SB and SC-CBF are measured at 1001 kN and 820 kN, respectively. This story shear distribution in SC-CBF-SB is likely attributed to the high-model effect that tends to amplify force demands in the bottom and top stories (Simpson 2020). Notably, the extra story shear is mainly undertaken by the SB system, and the story shear forces in the main frame of SC-CBF-SB are actually reduced; as a result, smaller inter-story drifts are observed in SC-CBF-SB, leading to reduced structural damage in comparison with SC-CBF.

Table 4 summarizes the maximum internal load demands in both SC-CBF and SC-CBF-SB. Columns in SC-CBF-SB experience smaller shear forces and bending moments compared to those in SC-CBF. In SC-CBF, the maximum shear force of 245 kN and bending moment of 631 kN·m are observed in the right column of the fifth and sixth stories, whereas the largest brace forces are observed in the first story with about 1926 kN in the left brace and 1903 kN in the right brace. By contrast, in SC-CBF-SB, relatively uniform distributions of shear force and bending moment demands are observed, with larger values

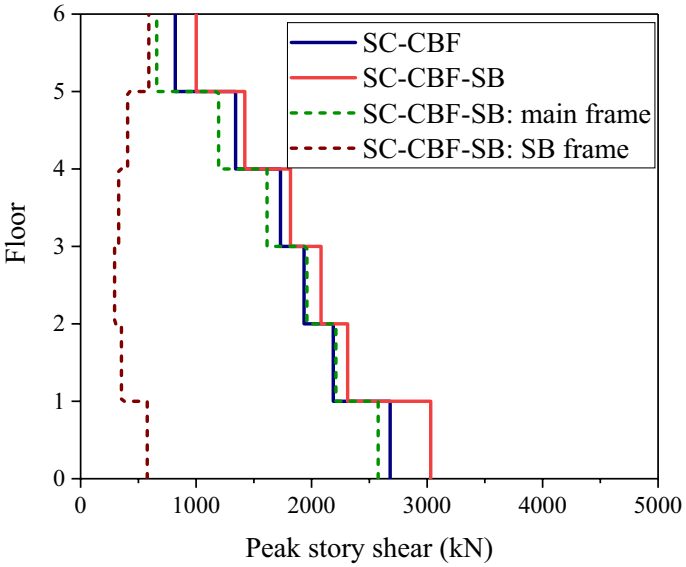

Fig. 14 Profile of peak story shear of SC-CBF and SC-CBF-SB subjected to LA27

in the bottom story and smaller values in the top story. The brace forces in the main frame of SC-CBF-SB are comparable to those of SC-CBF. As for the SB system, relatively larger axial force demands are observed in the diagonal members of the first and sixth stories.

Figure 15 compares the axial forces in the columns of SC-CBF and SC-CBF-SB. Apparently larger axial force demands are observed in the right column of SC-CBF-SB due to the installation of the adjacent SB system. To examine the effect of the SB system on the stability of columns, Fig. 16 shows the P-M interaction curve for the columns in SC-CBF and SC-CBF-SB. Under LA27, the maximum axial forces and bending moments of the left and right columns in the six stories of SC-CBF and SC-CBF-SB are collected, and the normalized axial forces and moments are plotted in Fig. 16. Compared with SC-CBF, the bending moments of the right and left columns in SC-CBF-SB are both smaller than those of SC-CBF. The axial forces of the columns in SC-CBF-SB are quite similar to SC-CBF for the left columns and are relatively higher for the right column. Considering the small magnitude of the bending moments and axial forces in the right columns, the addition of the SB system does not produce a negative effect on the column stability in SC-CBF-SB.

7.2 Performance evaluation under multiple ground motions

As aforementioned, two sets of ground motions representing DBE (LA01-LA20) and MCE (LA21-LA40) levels are used as seismic excitations. Figure 17 compares the profiles of the peak inter-story drift ratios of SC-CBF and SC-CBF-SB frame under the DBE ground motions, and the corresponding arithmetic means of each story under 20 ground motions are also calculated for SC-CBF and SC-CBF-SB. Under the DBE ground motions, the maximum peak inter-story drift ratio of about 1.5% is observed in the sixth story of SC-CBF. In comparison, the profile of peak inter-story drift ratios is relatively uniform in

Table 4 Maximum internal loads in the SC-CBF and SC-CBF-SB under LA27 (the numbers outside and inside the brackets show the internal loads of the left and right elements, respectively)

Story	SC-CBF Left (right)				SC-CBF-SB Left (Right)					
	Column			Brace Axial (kN)	Column			Brace Axial (kN)	SB	
	Axial (kN)	Shear (kN)	Moment (kN-m)		Axial (kN)	Shear (kN)	Moment (kN-m)		Diagonal member—Axial (kN)	Vertical member -Axial (kN)
1	3424 (3420)	106 (110)	398 (463)	1926 (1903)	3414 (4026)	91 (85)	273 (176)	1905 (1887)	1905	–
2	2488 (2486)	129 (183)	470 (534)	1480 (1464)	2434 (3660)	100 (59)	259 (184)	1450 (1438)	917	1821
3	1662 (1660)	129 (234)	482 (581)	1305 (1293)	1626 (2945)	78 (58)	234 (178)	1282 (1272)	783	2348
4	942 (939)	126 (245)	498 (616)	1049 (1042)	909 (1982)	43 (40)	153 (119)	1061 (1054)	866	2604
5	390 (389)	136 (242)	497 (631)	804 (798)	333 (974)	32 (30)	140 (104)	786 (782)	1064	2492
6	4.29 (3.55)	132 (171)	482 (626)	458 (454)	34 (33)	31 (18)	107 (63)	435 (433)	1616	1513

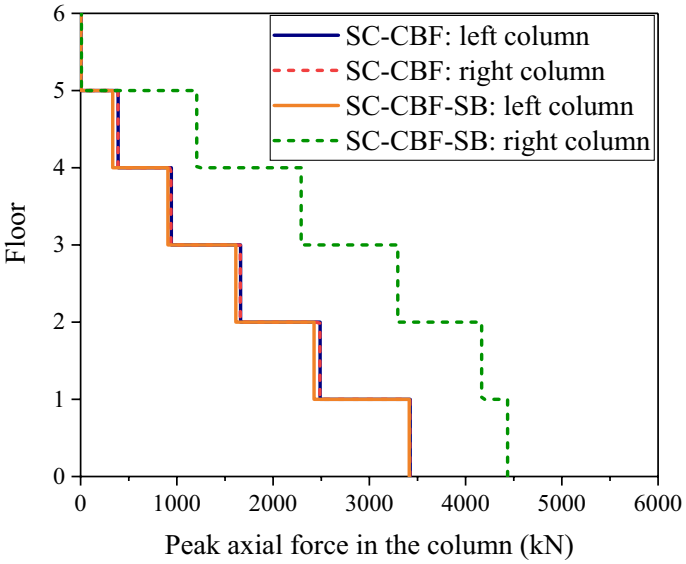

Fig. 15 Profile of peak axial force in the columns of SC-CBF and SC-CBF-SB subjected to LA27

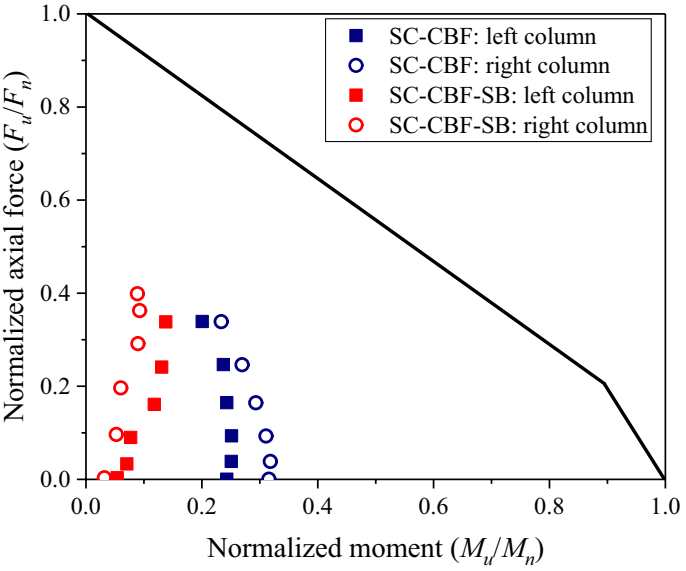

Fig. 16 P-M interaction curves with the normalized axial forces and bending moments in the columns of SC-CBF and SC-CBF-SB under LA27

SC-CBF-SB: the peak inter-story drift ratios are 1.1%, 1.1%, 1.0%, 1.0%, 1.1%, and 1.1% from the first to sixth stories.

Figure 18 compares the profiles of arithmetic means of the peak inter-story drift ratios of SC-CBF and SC-CBF-SB under the MCE (LA21-LA40) ground motions. Weak stories

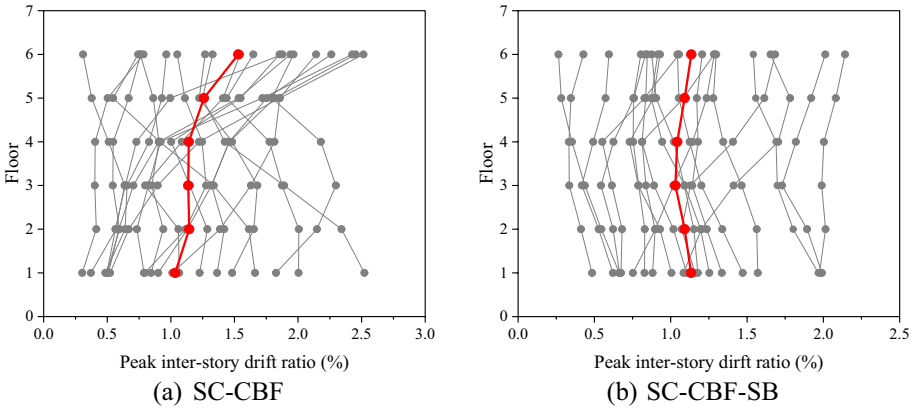

Fig. 17 Profile of peak inter-story drifts subjected to DBE

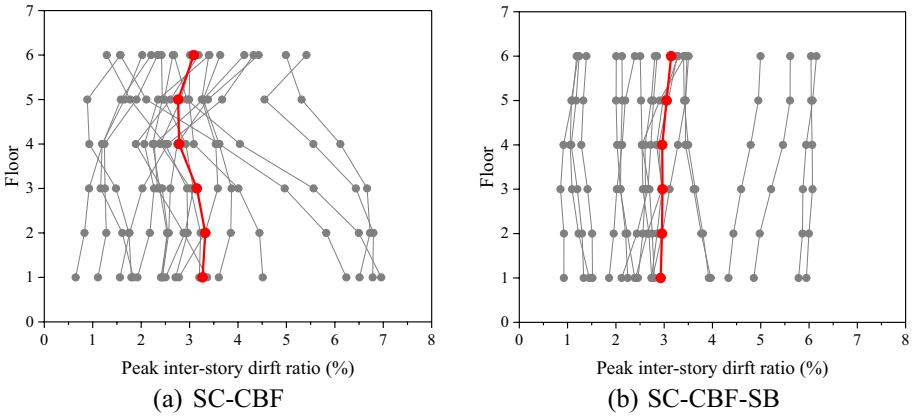

Fig. 18 Profile of peak inter-story drifts subjected to MCE

occur in the bottom and upper stories of SC-CBF, and relatively larger values of inter-story drift ratios are observed in the second and sixth stories, reaching 3.3% and 3.1%, respectively. For SC-CBF-SB, the arithmetic means of 3.1% peak inter-story drift ratio is observed in the sixth story. Generally, SC-CBF-SB still exhibited a more uniform distribution of inter-story drift ratio under the MCE ground motions.

Figure 19a further compares the maximum inter-story drift ratios of SC-CBF and SC-CBF-SB under the DBE ground motions, where the maximum values are picked out from the inter-story drift ratios among six stories. The mean values of the maximum inter-story drift ratios of SC-CBF and SC-CBF-SB are 1.73% and 1.28%, respectively. Figure 19b compares the maximum inter-story drift ratios under the MCE ground motions. Similar observations can be made. The mean values of the maximum inter-story drift ratios of SC-CBF and SC-CBF-SB are 3.92% and 3.25%, respectively. In general, SC-CBF-SB can achieve considerably smaller maximum inter-story drift ratios under both DBE and MCE levels. Notably, the maximum roof drift ratios of SC-CBF and SC-CBF-SB are very close to each other: they are 1.00% and 1.01%, respectively,

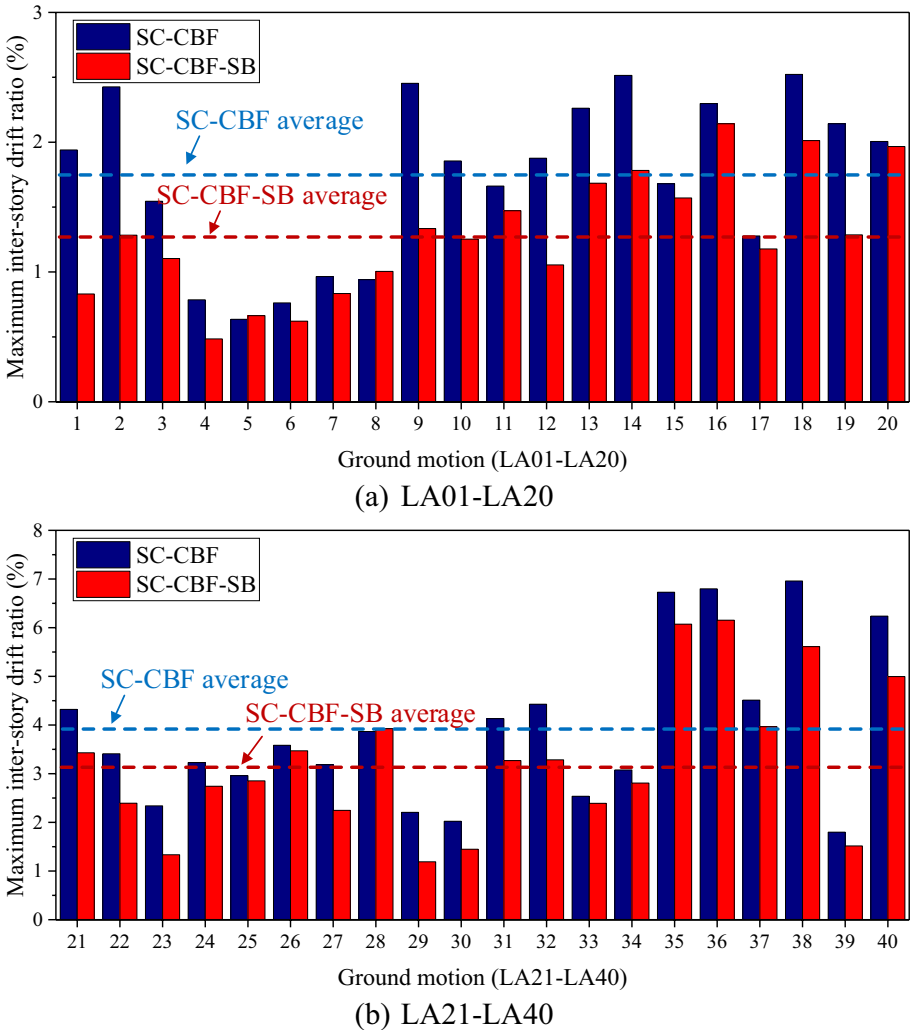

Fig. 19 Maximum inter-story drift ratios of SC-CBF and SC-CBF-SB under **a** DBE and **b** MCE

under the DBE level, and are 2.68% and 2.89%, respectively, under the MCE level. The roof drift ratios of the frames are typically dominated by the first-mode responses. As explained before, the SB system does not have a noticeable impact on the first-mode frequency and mode shapes. The close roof drift ratios imply that the higher maximum inter-story drift ratios observed in SC-CBF are mainly due to the non-uniform distributions of inter-story drift ratios along the frame height. Compared with the roof drift ratios, the inter-story drift ratios are more obviously affected by the inter-story deformation concentration, in which the SB system plays a more important role, as discussed in Sect. 5.

To further assess the distribution uniformity, the variability of the inter-story drift ratios among six stories of SC-CBF and SC-CBF-SB under each individual ground motion is quantified through the following standard deviation:

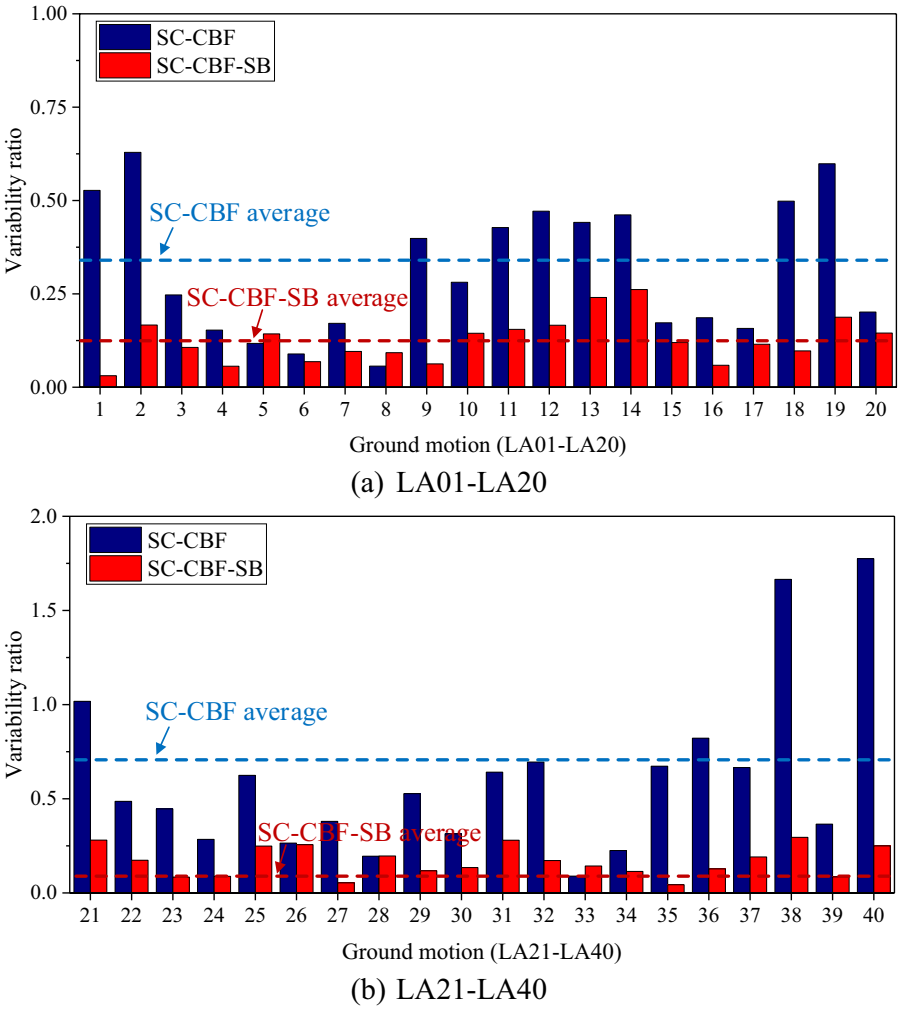

Fig. 20 σ_{story} of SC-CBF and SC-CBF-SB subjected to DBE and MCE

$$\sigma_{story} = \sqrt{\frac{\sum\left(\theta_{i,peak} - \overline{\theta}_{i,peak}\right)}{N}}, i = 1, 2, \ldots 6 \tag{1}$$

where $\theta_{i,peak}$ is defined as the peak inter-story drift ratio of the i^{th} story, and $\overline{\theta}_{i,peak}$ is defined as the mean of the peak inter-story drift ratios among six stories. A smaller σ_{story} indicates a reduced discrepancy among inter-story drift ratios of different stories. Figure 20a and b compare σ_{story} of SC-CBF and SC-CBF-SB subjected to the DBE and MCE ground motions, respectively. The mean values of σ_{story} of SC-CBF and SC-CBF-SB are 0.31 and 0.12, respectively, under the DBE level, and are 0.61 and 0.17, respectively, under the MCE level. Generally, σ_{story} of SC-CBF-SB is considerably smaller than that of SC-CBF, indicating a more uniform profile of inter-story drift ratios.

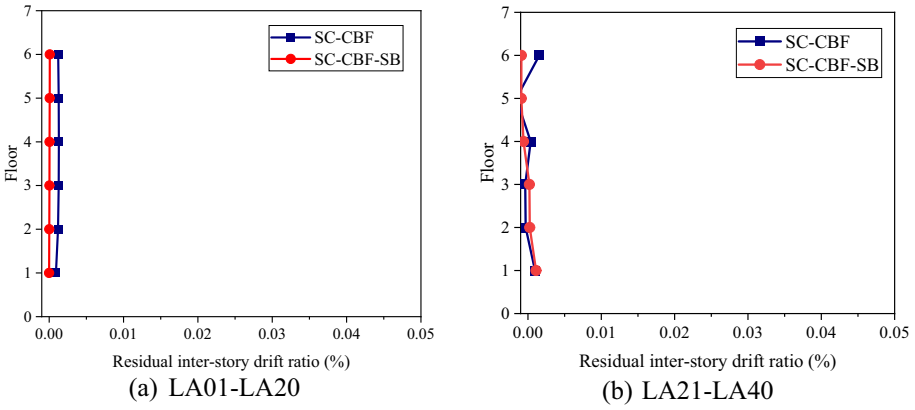

Fig. 21 Mean value of residual inter-story drift ratios of SC-CBF and SC-CBF-SB

Figure 21 illustrates the mean values of the residual inter-story drift ratios of SC-CBF and SC-CBF-SB subjected to the DBE and MCE ground motions. Negligible residual drift ratios are observed in both SC-CBF and SC-CBF-SB under both levels, meaning that the SB system, if properly designed, will not diminish the SC ability of the frame.

8 IDA analysis

IDA is often adopted to estimate structural performance subjected to varying seismic intensities (Vamvatsikos and Cornell 2002). IDA is also conducted with 20 ground motions (LA01-LA20) to investigate seismic performance of SC-CBF and SC-CBF-SB, in which each seismic motion record is scaled independently by using the spectral acceleration at the fundamental periods of the frames with 5% damping $S_a(T_1,5\%)$ as the intensity measure (IM). Figure 22a illustrates the IDA curves for the maximum roof drift ratios of SC-CBF and SC-CBF-SB, where three curves correspond to the 16th,

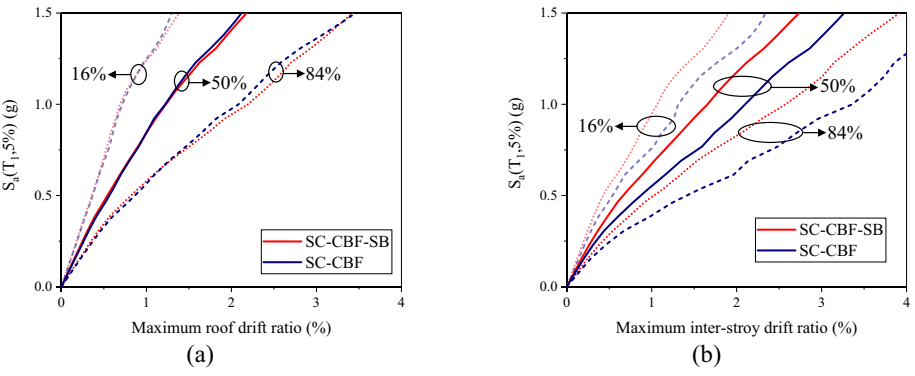

Fig. 22 IDA curves for **a** maximum roof drift and **b** maximum inter-story drift ratio of SC-CBF as well as SC-CBF-SB at varying seismic intensity levels

50th, and 84th percentiles of the peak roof drift ratios, respectively. The IDA curves for the roof drift ratios of SC-CBF and SC-CBF-SB are almost identical. Figure 22b illustrates the IDA curves for the maximum inter-story drift ratios of SC-CBF and SC-CBF-SB. Unlike the roof drift response, SC-CBF-SB exhibits considerably smaller inter-story drift deformation demands than SC-CBF. With the increasing seismic intensity level, the gap between SC-CBF and SC-CBF-SB also increases.

The drift concentration factor (DCF) is another indicator to evaluate the uniformity of inter-story drift distributions (Qu et al. 2014). DCF can be calculated as the maximum inter-story drift divided by the roof drift:

$$DCF_n = \frac{\theta_{\max,n}}{\theta_{roof,n}} \tag{2}$$

where $\theta_{max,n}$ is defined as the maximum inter-story drift of the frame under the n^{th} ground motion, and $\theta_{roof,n}$ is defined as the roof drift of the frame under the n^{th} ground motion. Given a uniform profile of inter-story drifts, DCF_n should be close to 1, meaning that maximum inter-story drift equals roof drift. A higher mean value of DCF_n indicates a larger discrepancy between the maximum inter-story drift and the roof drift, reflecting a less uniform distribution of inter-story drifts. Figure 23 compares the IDA curves of the mean *DCF* value of SC-CBF and SC-CBF-SB. Results show that when $S_a(T_1,5\%)$ is below 0.8 g, the increasing seismic intensity results in an increase of *DCF* for both SC-CBF and SC-CBF-SB. This signifies the growing gaps between the roof drift and maximum inter-story drift. The maximum value of *DCF* is about 1.3 and 1.8 for SC-CBF-SB and SC-CBF respectively. In general, the *DCF* ratio of SC-CBF-SB is considerably lower than that of SC-CBF, indicating that the discrepancy is less pronounced in SC-CBF-SB. Meanwhile, a higher growth rate of *DCF* is observed in SC-CBF when the seismic intensity increases from 0.2 to 0.75 g, implying that the inter-story drift ratios of SC-CBF become more nonuniform with the increasing seismic intensity.

The performance of both SC-CBF and SC-CBF-SB is further investigated through probabilistic seismic fragility analysis. The IDA data is used to generate the corresponding fragility curves. The probability of exceedance can be calculated as below:

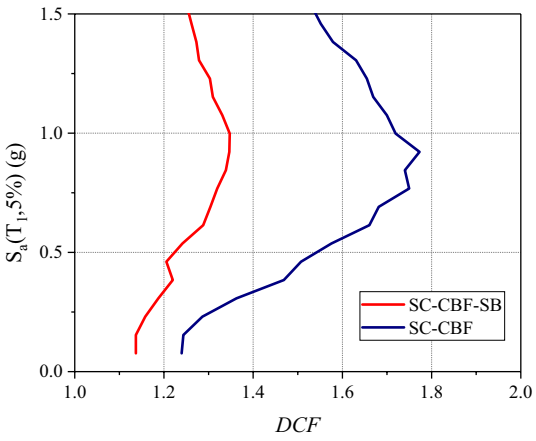

Fig. 23 IDA curves of mean value of *DCF* of SC-CBF and SC-CBF-SB at varying seismic intensity levels

$$P\left[\theta_{\max} > \theta_{\max,L} \middle| S_a\right] = 1 - \Phi\left[\frac{\ln\left(\theta_{\max,L}\right) - \ln\left(\widehat{\theta}_{\max}\right)}{\beta_{\theta_{\max}|S_a}}\right] \tag{3}$$

where $\Phi(\cdot)$ represents the cumulative distribution function of the standard normal distribution; $\widehat{\theta}_{\max}$ and $\beta_{\theta_{\max}|S_a}$ is the median and standard deviation of the natural logarithm distribution of $\theta_{\max}$ under a specific S_a. $\beta_{\theta_{\max}|S_a}$ can be calculated as:

$$\beta_{\theta_{\max}|S_a} = \sqrt{\frac{1}{n-1}\sum_{i=1}^{n}\left[\ln\left(\theta_{\max,i}|S_a\right) - \ln\left(\overline{\theta}_{\max}|S_a\right)\right]^2} \tag{4}$$

where n represents the number of earthquake records considered and $\theta_{\max,i}$ represents the maximum inter-story drift ratio under the i^{th} record, respectively.

Three levels of $\theta_{\max,L}$ which are 0.5%, 1.0% and 2% are defined as the limitations corresponding to three damage states: immediate occupancy, impaired occupancy, and structural damage (FEMA 1997). The probabilities of exceeding $\theta_{\max,L}$ when SC-CBF and SC-CBF-SB are subjected to different S_a are compared in Fig. 24. Generally, the probability of exceedance of the SC-CBF-SB is lower than that of SC-CBF through the whole IM range, illustrating the effectiveness of the SB system in controlling the maximum inter-story drift

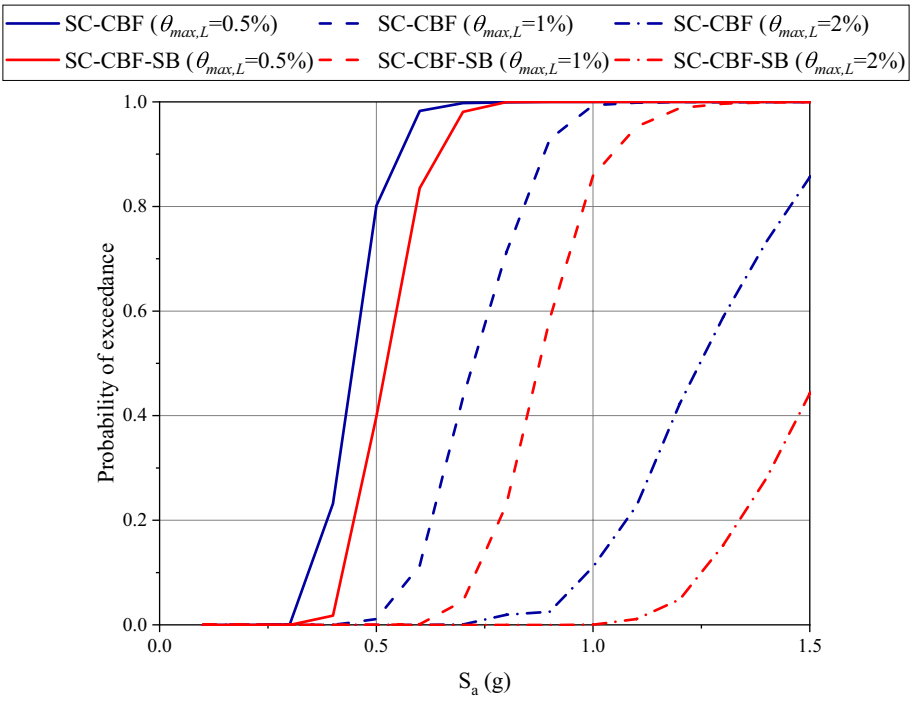

Fig. 24 Fragility curves of the inter-story drift ratios of SC-CBF and SC-CBF-SB

ratios. When the S_a reaches the DBE level (i.e., 0.76 g), the probabilities of exceeding the impaired occupancy limit are 0.75 and 0.29 for SC-CBF and SC-CBF-SB, respectively. When the S_a reaches the MCE level (i.e., 1.2 g), the probabilities of exceeding the structural damage limit are 0.58 and 0.12 for SC-CBF and SC-CBF-SB, respectively.

9 Conclusions

A novel SB system is proposed in this paper to mitigate the deformation concentration in weak stories in SC-CBFs. The SB system can be conveniently attached to an existing SC-CBF via pin connections to form a structural system called SC-CBF-SB. Comprehensive investigations into the fundamental principle and dynamic behavior of SC-CBF-SB are conducted. To fully compare the performance of SC-CBF and SC-CBF-SB, nonlinear static (i.e., pushover) and dynamic analyses are performed. The seismic performances of six-story SC-CBF and SC-CBF-SB are assessed under a single ground motion and under two sets of ground motions corresponding to the DBE and MCE levels. IDA is employed to evaluate the seismic performance of the frames under ground motions with continuously varying intensities. The following conclusions can be drawn based on the overall study results:

1. The original SC-CBF exhibits a uniform inter-story drift profile in the pushover analysis with the first-mode loading pattern. Considering that real seismic loads often deviate from the first-mode pattern, the pushover analyses with uniform and second-mode patterns are also performed, wherein the inter-story drift profiles of the SC-CBF become obviously non-uniform.
2. In both nonlinear static and dynamic analyses, the proposed SB system can effectively mitigate the weak-story behavior and promote uniform distributions of inter-story drift ratios in SC-SBF-SB.
3. In the pushover analyses, the SB system has a minimal effect under the first-mode loading pattern. However, when the loading pattern deviates from the first-mode pattern, or is dominated by a high mode, the SB system participates in the re-distribution of internal forces along the height and promotes more uniform inter-story drift profiles.
4. Compared with SC-CBF, SC-CBF-SB exhibits more uniform distributions of inter-story drifts under both DBE and MCE ground motions, with no obvious weak-story phenomenon being observed in SC-CBF-SB. The heightwise variability of inter-story drift ratios and the *DCF* are considerably reduced in SC-CBF-SB, compared with those in the original SC-CBF. The mean values of standard deviation σ_{story} of SC-CBF and SC-CBF-SB are 0.31 and 0.12, respectively, under the DBE level, and are 0.61 and 0.17, respectively, under the MCE level.
5. Owing to its more uniform inter-story drift distribution, SC-CBF-SB exhibits smaller maximum inter-story drift demands than SC-CBF. Under DBE ground motions, SC-CBF exhibits a maximum peak inter-story drift ratio of 1.5% in the sixth story, while SC-CBF-SB maintains a more uniform distribution with a maximum inter-story drift ratio of about 1.1%. Under MCE ground motions, SC-CBF exhibits weak stories in the second story with a peak drift ratio of 3.3%, while SC-CBF-SB exhibits a uniform distribution of the inter-story drift ratio with a maximum value of 3.1% in the sixth story.

Meanwhile, the incorporation of the SB system exerts a minimal effect on the SC ability of the frame.

6. The IDA results demonstrate that with increasing seismic intensity, the inter-story drift concentration in SC-CBF becomes more significant, and the difference in the *DCF* between SC-CBF and SC-CBF-SB also increases. The maximum value of *DCF* is about 1.3 and 1.8 for SC-CBF-SB and SC-CBF respectively. Meanwhile, seismic fragility analysis revealed that the probability of exceedance of multiple inter-story drift limits for the SC-CBF-SB is considerably lower than that of SC-CBF, illustrating the effectiveness of the SB system.

Numerical results presented in this paper demonstrate the prospects of the SB system in mitigating the concentration of inter-story drift ratios in SC-CBF. Systematic experimental work is still needed in the future to validate the seismic performance of SC-CBF-SB. Meanwhile, developing an ad hoc performance-based design approach for the proposed SC-CBF-SB is crucial to promote the practical adoption of the SB systems in real construction projects.

Appendix: Comparative study on three-story SC-CBF and SC-CBF-SB

In addition to the six-story SC-CBF, this study also comparatively investigated the performance of three-story SC-CBF and SC-CBF-SB. Because the major conclusions are similar to those for the six-story SC-CBF, these results are provided in this Appendix for further reference.

Figure 25 presents the elevation view of the three-story SC-CBF and SC-CBF-SB. Both the three-story and six-story frames have been adopted in the previous research (Sabelli 2001; Qiu et al. 2022). Table 5 presents the member sizes of the three-story SC-CBF and SB system. Other detailed information regarding the frame design can be obtained from the reference (Qiu et al. 2022). Similar to Sect. 8, nonlinear time history analyses of the three-story SC-CBF and SC-CBF-SB under the single ground motion and multiple ground motions were also conducted, and the corresponding results are presented in this Appendix. The multiple natural periods of the SC-CBF and SC-CBF-SB are listed in the Table 6. The first modal period of three-story SC-CBF is approximately 0.38 s, which is quite close to the first modal period of SC-CBF-SB at approximately 0.37 s.

Figure 26 shows the time histories of inter-story drift ratios of three stories in SC-CBF and SC-CBF-SB when subjected to the ground motion LA27. Only 15-s time histories that cover the peak values of inter-story drifts are presented to have a clear view of details in the frame responses. The occurrence time of the peak inter-story drifts is marked as well. In SC-CBF, it is evident that the inter-story drifts of different stories differ considerably,

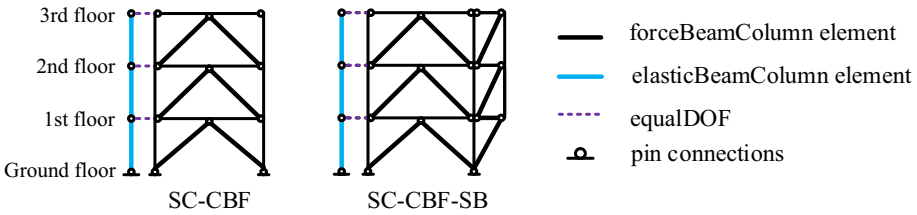

Fig. 25 FE models of three-story SC-CBF and SC-CBF-SB

Table 5 Member sizes of three-story SC-CBF and SB system

Story	SC-CBF					SB system		
	Columns	Beams	Braces			Vertical members	Horizontal members	Diagonal members
			F_y (kN)	k_i (kN /m)	Area (mm^2)			
3	W12×96	W14×48	1161	2.165E+05	4681	W12×96	W14×48	W12×96
2	W12×96	W14×48	1306	2.435E+05	5237	W12×96	W14×48	W12×96
1	W12×96	W14×48	1704	2.878E+05	6851	–	W14×48	W12×96

Table 6 Fundamental periods of three-story SC-CBF and SC-CBF-SB

	T_1 (s)	T_2 (s)	T_3 (s)
SC-CBF	0.38	0.16	0.12
SC-CBF-SB	0.37	0.15	0.12

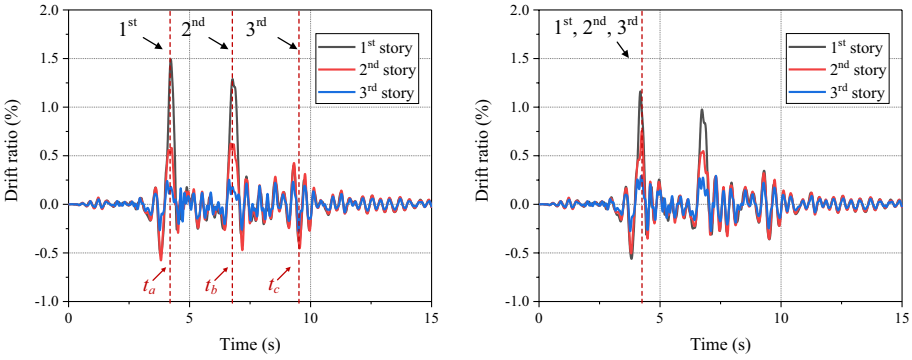

(a) Three-story SC-CBF (b) Three-story SC-CBF-SB

Fig. 26 Time history of inter-story drift ratio of three-story frames under the ground motion LA27

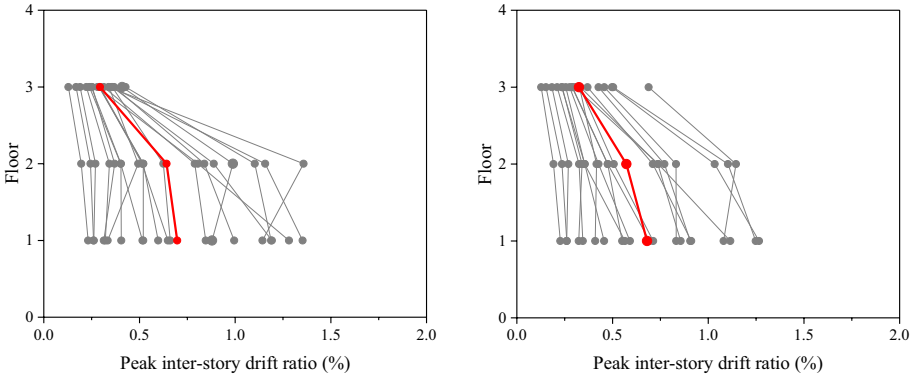

(a) SC-CBF (b) SC-CBF-SB

Fig. 27 Profile of peak inter-story drifts of three-story frames subjected to DBE

and the peak inter-story drift ratios of different stories do not occur simultaneously. Specifically, the inter-story drifts of the first, second and third stories reach their peak values at around t_a=4.2 s, t_b=6.7 s and t_c=9.5 s, respectively. By contrast, in SC-CBF-SB, the inter-story drifts for all three stories are very close and reach their maximum values nearly at the same instant of t_a=4.2 s.

Figure 27 compares the profiles of the peak inter-story drift ratios of three-story SC-CBF and SC-CBF-SB frame under the DBE ground motions, and the corresponding arithmetic means of each story under 20 ground motions are also calculated for SC-CBF and SC-CBF-SB. Under the DBE ground motions, the maximum peak inter-story drift ratio of

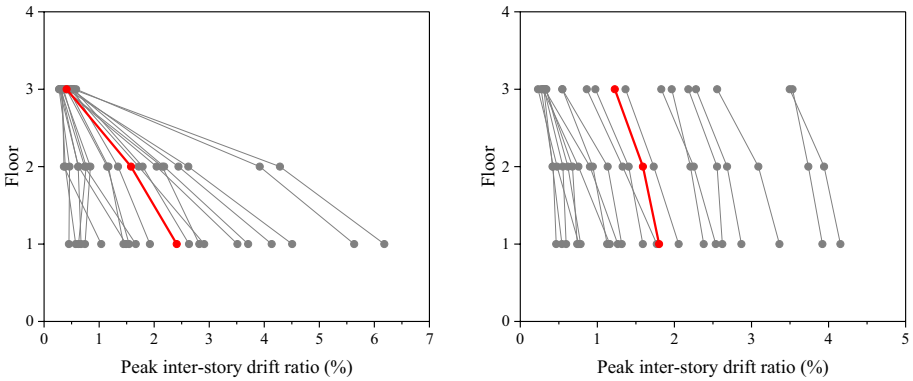

Fig. 28 Profile of peak inter-story drifts of three-story frames subjected to MCE

about 0.70% is observed in the first story of SC-CBF. In comparison, the maximum peak inter-story drift ratio of SC-CBF-SB is 0.68%. Figure 28 compares the profiles of arithmetic means of the peak inter-story drift ratios of three-story SC-CBF and SC-CBF-SB under the MCE (LA21-LA40) ground motions. Weak stories occur in the bottom story of SC-CBF, and relatively larger values of inter-story drift ratios are observed in the first story, reaching 2.4%. For SC-CBF-SB, the arithmetic means of 1.8% peak inter-story drift ratio is observed in the first story. Generally, SC-CBF-SB still exhibited a more uniform distribution of inter-story drift ratio under the MCE ground motions.

Figure 29a further compares the maximum inter-story drift ratios of SC-CBF and SC-CBF-SB under the DBE ground motions. The mean values of the maximum inter-story drift ratios of SC-CBF and SC-CBF-SB are 0.72% and 0.68%, respectively. Figure 29b compares the maximum inter-story drift ratios under the MCE ground motions. Similar observations can be made. The mean values of the maximum inter-story drift ratios of SC-CBF and SC-CBF-SB are 2.42% and 1.80%, respectively. In general, SC-CBF-SB can achieve considerably smaller maximum inter-story drift ratios under both DBE and MCE levels.

Figures 30a and b compare σ_{story} of SC-CBF and SC-CBF-SB subjected to the DBE and MCE ground motions, respectively. The mean values of σ_{story} of SC-CBF and SC-CBF-SB are 0.19 and 0.15, respectively, under the DBE level, and are 0.84 and 0.24, respectively, under the MCE level. Generally, σ_{story} of SC-CBF-SB is considerably smaller than that of SC-CBF, indicating a more uniform profile of inter-story drift ratios.

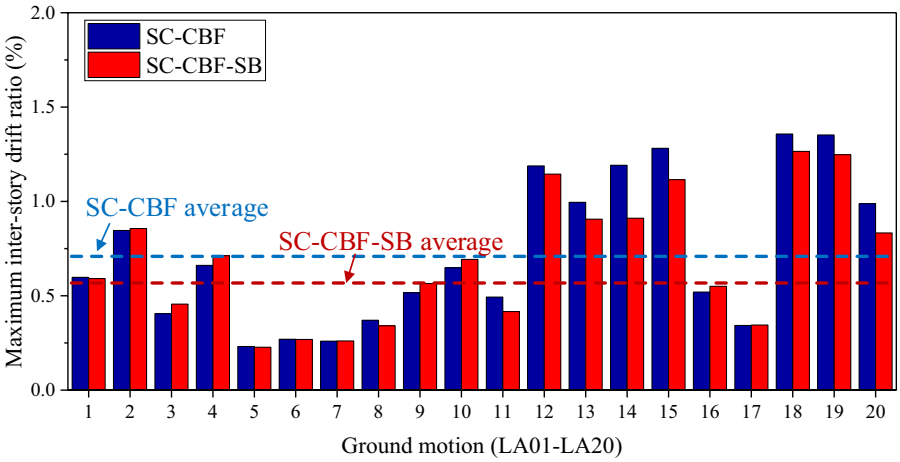

(a) LA01-LA20

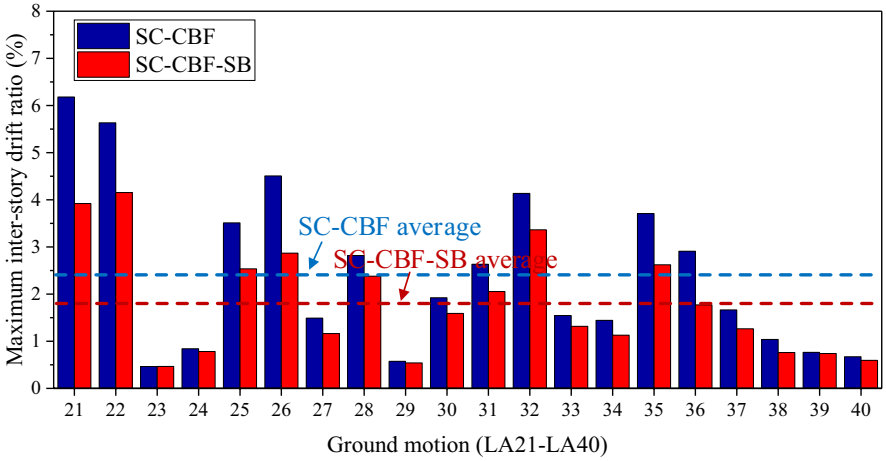

(b) LA21-LA40

Fig. 29 Maximum inter-story drift ratios of three-story SC-CBF and SC-CBF-SB under **a** DBE and **b** MCE

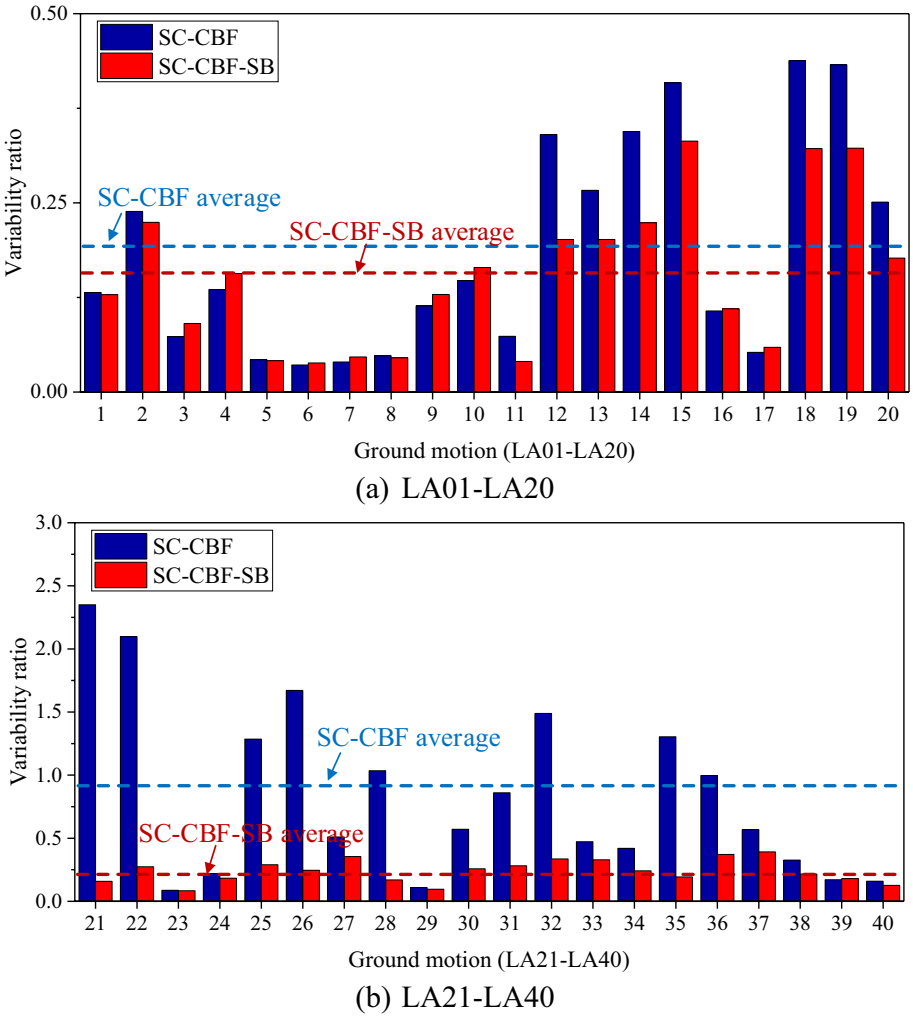

Fig. 30 σ_{story} of three-story SC-CBF and SC-CBF-SB subjected to DBE and MCE

Funding Open access funding provided by The Hong Kong Polytechnic University. The authors are grateful for the financial support from the Research Grants Council of Hong Kong through a GRF Project (Grant No. 15231723), the Hong Kong Polytechnic University (Grant Nos. U-CDB6, 1-W02L, 1-CDKN), the Hong Kong Branch of National Rail Transit Electrification and Automation Engineering Technology Research Center (Grant No. K-BBY1). The first author acknowledges the financial support from the Hong Kong PhD Fellowship Scheme. The findings and opinions expressed in this work are solely those of the authors and do not represent the views of the sponsors.

Declarations

Conflict of interest The authors declare that they have no known competing financial interests or personal relationships that could have appeared to influence the work reported in this paper.

References

Aiken ID, Mahin SA, Uriz P (2002) Large-scale testing of buckling-restrained braced frames. Japan Passive Control Symposium, Tokyo Institute of Technology Yokohama, Japan.

Asadolahi SM, Fanaie N (2020) Performance of self-centering steel moment frame considering stress relaxation in prestressed cables. Adv Struct Eng 23(9):1813–1822

Casciati F, Faravelli L, Hamdaoui K (2007) Performance of a base isolator with shape memory alloy bars. Earthq Eng Eng Vib 6(4):401–408

Chen Z-P, Zhu S (2024) Cyclic tension–compression behaviours of large-dimensional superelastic shape memory alloy buckling-restrained plates. Journal of Structural Engineering.

Chi H, Liu J (2012) Seismic behavior of post-tensioned column base for steel self-centering moment resisting frame. J Constr Steel Res 78:117–130

Christopoulos C, Tremblay R, Kim H-J, Lacerte M (2008) Self-centering energy dissipative bracing system for the seismic resistance of structures: development and validation. J Struct Eng 134(1):96–107

Di Sarno L, Elnashai AS (2009) Bracing systems for seismic retrofitting of steel frames. J Constr Steel Res 65(2):452–465

Dolce M, Cardone D, Ponzo FC, Valente C (2005) Shaking table tests on reinforced concrete frames without and with passive control systems. Earthq Eng Struct Dyn 34(14):1687–1717

Dolce M, Cardone D, Ponzo FC (2007) Shaking-table tests on reinforced concrete frames with different isolation systems. Earthq Eng Struct Dyn 36(5):573–596

Eatherton MR, Ma X, Krawinkler H, Mar D, Billington S, Hajjar JF, Deierlein GG (2014) Design concepts for controlled rocking of self-centering steel-braced frames. J Struct Eng 140(11):04014082

Ebrahimi Majumerd MJ, Mohammadi Dehcheshmeh E, Broujerdian V, Laghi V, Palermo M (2023) Introducing a base-rocking dual-core braced-frame system equipped with vertical buckling-restrained fuses. Bull Earthq Eng 21(14):6453–6476

Erochko J, Christopoulos C, Tremblay R, Kim HJ (2013) Shake table testing and numerical simulation of a self-centering energy dissipative braced frame. Earthq Eng Struct Dyn 42(11):1617–1635

Fahnestock LA, Sause R, Ricles JM (2007) Seismic response and performance of buckling-restrained braced frames. J Struct Eng 133(9):1195–1204

FEMA 356, FE (2000) Prestandard and commentary for the seismic rehabilitation of buildings. Federal emergency management agency: Washington, DC, USA.

FEMA (1997) Nehrp guidelines for the seismic rehabilitation of buildings (fema 273). Building Seismic Safety Council: Washington, DC, USA.

Garlock MM, Ricles JM, Sause R (2005) Experimental studies of full-scale posttensioned steel connections. J Struct Eng 131(3):438–448

Goel RK, Chopra AK (2004) Evaluation of modal and FEMA pushover analyses: SAC buildings. Earthq Spectra 20(1):225–254

Hu S, Koetaka Y, Chen Z-P, Zhu S, Alam MS (2024) Hybrid self-centering braces with NiTi-SMA U-shaped and frequency-dependent viscoelastic dampers for structural and nonstructural damage control. Eng Struct 308:117920

Lai J-W, Mahin SA (2015) Strongback system: a way to reduce damage concentration in steel-braced frames. J Struct Eng 141(9):04014223

Lavaei MH, Dehcheshmeh EM, Safari P, Broujerdian V, Gandomi AH (2023) Reliability-based design optimization of post-tensioned self-centering rocking steel frame structures. J Build Eng 75:106955

Li HN, Huang Z, Fu X, Li G (2018) A re-centering deformation-amplified shape memory alloy damper for mitigating seismic response of building structures. Struct Control Health Monit 25(9):e2233

Lin Z, Xu L, Xie X (2022) Development and seismic performance improvement of hybrid damping self-centering braced frame. Journal of Building Engineering 52:104388

McCormick J, DesRoches R, Fugazza D, Auricchio F (2007) Seismic assessment of concentrically braced steel frames with shape memory alloy braces. J Struct Eng 133(6):862–870
McCormick J, Aburano H, Ikenaga M, Nakashima M (2008). Permissible residual deformation levels for building structures considering both safety and human elements. In: Proceedings of the 14th world conference on earthquake engineering, Seismological Press Beijing.
Miller DJ, Fahnestock LA, Eatherton MR (2012) Development and experimental validation of a nickel–titanium shape memory alloy self-centering buckling-restrained brace. Eng Struct 40:288–298
OpenSees S (2013). Open system for earthquake engineering simulation (OpenSees), Pacific earthquake engineering research center, Berkeley, CA.
Pollino M, Slovenec D, Qu B, Mosqueda G (2017) Seismic rehabilitation of concentrically braced frames using stiff rocking cores. J Struct Eng 143(9):04017080
Qiu C-X, Zhu S (2016a) High-mode effects on seismic performance of multi-story self-centering braced steel frames. J Constr Steel Res 119:133–143
Qiu C, Zhu S (2017) Shake table test and numerical study of self-centering steel frame with SMA braces. Earthq Eng Struct Dyn 46(1):117–137
Qiu C, Liu J, Du X (2022) Cyclic behavior of SMA slip friction damper. Eng Struct 250:113407
Qu B, Guo X, Pollino M, Chi H (2013) Effect of column stiffness on drift concentration in steel plate shear walls. J Constr Steel Res 83:105–116
Qu B, Sanchez-Zamora F, Pollino M (2014) Mitigation of inter-story drift concentration in multi-story steel concentrically braced frames through implementation of rocking cores. Eng Struct 70:208–217
Qu B, Sanchez-Zamora F, Pollino M (2015) Transforming seismic performance of deficient steel concentrically braced frames through implementation of rocking cores. J Struct Eng 141(5):04014139
Razavi M, Fanaie N (2023) Investigation of the performance of the self-centering steel plate shear wall considering stress relaxation in pre-stressed cables. Structures. Elsevier, Amsterdam
Ricles JM, Sause R, Peng S, Lu L (2002) Experimental evaluation of earthquake resistant posttensioned steel connections. J Struct Eng 128(7):850–859
Sabelli R, Mahin S, Chang C (2003) Seismic demands on steel braced frame buildings with buckling-restrained braces. Eng Struct 25(5):655–666
Sabelli R (2001) Research on improving the design and analysis of earthquake-resistant steel-braced frames, EERI Oakland, CA, USA.
Simpson BG (2020) Higher-mode force response in multi-story strongback-braced frames. Earthq Eng Struct Dyn 49(14):1406–1427
Simpson BG, Mahin SA (2018) Experimental and numerical investigation of strongback braced frame system to mitigate weak story behavior. J Struct Eng 144(2):04017211
Simpson BG, Rivera Torres D (2021) Simplified modal pushover analysis to estimate first-and higher-mode force demands for design of strongback-braced frames. J Struct Eng 147(12):04021196
Slovenec D, Sarebanha A, Pollino M, Mosqueda G, Qu B (2017) Hybrid testing of the stiff rocking core seismic rehabilitation technique. J Struct Eng 143(9):04017083
Somerville PG (1997) Development of ground motion time histories for phase 2 of the FEMA/SAC steel project, SAC Joint Venture.
Speicher MS, DesRoches R, Leon RT (2011) Experimental results of a NiTi shape memory alloy (SMA)-based recentering beam-column connection. Eng Struct 33(9):2448–2457
Tremblay R, Archambault M-H, Filiatrault A (2003) Seismic response of concentrically braced steel frames made with rectangular hollow bracing members. J Struct Eng 129(12):1626–1636
Uriz P, Mahin SA (2008) Towards earthquake resistant design of concentrically braced steel structures. PEER report 2008/08, Earthquake Engineering Research Center, University of California, Berkeley.
Vamvatsikos D, Cornell CA (2002) Incremental dynamic analysis. Earthq Eng Struct Dyn 31(3):491–514
Wang B, Zhu S, Casciati F (2020) Experimental study of novel self-centering seismic base isolators incorporating superelastic shape memory alloys. J Struct Eng 146(7):04020129
Wang W, Fang C, Shen D, Zhang R, Ding J, Wu H (2021) Performance assessment of disc spring-based self-centering braces for seismic hazard mitigation. Eng Struct 242:112527
Wang Y, Zhou Z, Xie Y, Huang L (2023) Theoretical model to predict the seismic drift concentration effect for self-centering-braced frame. J Constr Steel Res 207:107950
Watanabe A, Hitomi Y, Saeki E, Wada A, Fujimoto M (1988) Properties of brace encased in buckling-restraining concrete and steel tube. In: Proceedings of 9th world conference on earthquake engineering.
Wolski M, Ricles JM, Sause R (2009) Experimental study of a self-centering beam–column connection with bottom flange friction device. J Struct Eng 135(5):479–488
Zhang R, Wang W, Alam MS (2022) Performance-based seismic design of full and partial self-centering steel braced frames using modified lateral force distribution. J Constr Steel Res 196:107438

Zhu S, Zhang Y (2007) Seismic behaviour of self-centring braced frame buildings with reusable hysteretic damping brace. Earthq Eng Struct Dyn 36(10):1329–1346
Zhu S, Zhang Y (2008) Seismic analysis of concentrically braced frame systems with self-centering friction damping braces. J Struct Eng 134(1):121–131